Astronomy & Astrophysics manuscript no. mrk273_printer_accepted
October 29, 2018

Molecular gas in the northern nucleus of Mrk 273: Physical and chemical properties of the disk and its outflow

R. Aladro[1,2], S. König[2], S. Aalto[2], E. González-Alfonso[3], N. Falstad[2], S. Martín[4,5], S. Muller[2], S. García-Burillo[6], C. Henkel[1,7], P. van der Werf[8], E. Mills[9], J. Fischer[10], F. Costagliola[2], and M. Krips[11]

[1] Max-Planck-Institut für Radioastronomie, Auf dem Hügel 69, 53121, Bonn, Germany
e-mail: aladro@mpifr-bonn.mpg.de
[2] Chalmers University of Technology, Department of Space, Earth and Environment, Onsala Space Observatory, 43992 Onsala, Sweden
[3] Universidad de Alcalá, Departamento de Física y Matemáticas, Campus Universitario, 28871 Alcalá de Henares, Madrid, Spain
[4] European Southern Observatory, Alonso de Córdova 3107, Vitacura 763 0355, Santiago, Chile
[5] Joint ALMA Observatory, Alonso de Córdova 3107, Vitacura 763 0355, Santiago, Chile
[6] Observatorio de Madrid, OAN-IGN, Alfonso XII, 3, E-28014-Madrid, Spain
[7] Astron. Dept., King Abdulaziz University, P.O. Box 80203, 21589 Jeddah, Saudi Arabia
[8] Leiden Observatory, Leiden University, P.O. Box 9513, NL-2300 RA Leiden, The Netherlands
[9] San Jose State University, 1 Washington Square, San Jose, CA 95192, USA
[10] George Mason University, Department of Physics & Astronomy, MS 3F3, 4400 University Drive, Fairfax, VA 22030, USA
[11] Institut de Radio Astronomie Millimétrique, 300 rue de la Piscine, Dom. Univ., 38406 St Martin d'Hères, France

Received ; accepted

ABSTRACT

Aiming to characterise the properties of the molecular gas in the ultraluminous infrared galaxy Mrk 273 and its outflow, we used the NOEMA interferometer to image the dense gas molecular tracers HCN, HCO^+, HNC, HOC^+ and HC_3N at ~86 GHz and ~256 GHz with angular resolutions of 4.″9×4.″5 (~3.7×3.4 kpc) and 0.″61×0.″55 (~460×420 pc). We also modelled the flux of several H_2O lines observed with *Herschel* using a radiative transfer code that includes excitation by collisions as well as by far-infrared photons. The disk of the Mrk 273 north nucleus has two components with decoupled kinematics. The gas in the outer parts (R~1.5 kpc) rotates with a south-east to north-west direction, while in the inner disk (R~300 pc) follows a north-east to south-west rotation. The central 300 pc, which hosts a compact starburst region, is filled with dense and warm gas, and contain a dynamical mass of $(4-5)\times10^9 M_\odot$, a luminosity of $L'_{\rm HCN} = (3-4)\times10^8$ K km s^{-1}pc^2, and a dust temperature of 55 K. At the very centre, a compact core with R~50 pc has a luminosity of $L_{\rm IR} = 4\times10^{11} L_\odot$ (30% of the total infrared luminosity), and a dust temperature of 95 K . The core is expanding at low velocities ~50-100 km s^{-1}, probably affected by the outflowing gas. We detect the blue-shifted component of the outflow, while the red-shifted counterpart remains undetected in our data. Its cold and dense phase reaches fast velocities up to ~1000 km s^{-1}, while the warm outflowing gas has more moderate maximum velocities of ~600 km s^{-1}. The outflow is compact, being detected as far as 460 pc from the centre in the northern direction, and has a mass of dense gas $\leq 8\times10^8 M_\odot$. The difference between the position angles of the inner disk (~70°) and the outflow (~10°) indicates that the outflow is likely powered by the AGN, and not by the starburst. Regarding the chemistry in Mrk 273, we measure an extremely low HCO^+/HOC^+ ratio of 10±5 in the inner disk of Mrk 273.

Key words. galaxies: individual: Mrk 273 - galaxies: nuclei -ISM: molecules - line: profiles - Astrochemistry - Galaxies: kinematics and dynamics

1. Introduction

Tracers of dense molecular gas are good probes of the central regions of active galaxies, where molecular regions are subjected to strong radiation fields (X-rays, cosmic rays and UV fields) created by massive star formation and/or active galactic nuclei (AGNs). In particular, the rotational transitions of HCN and HCO^+ have bright emission and high dipole moment (hence large critical density) and are thus convenient tracers of the dense gas component in galactic centres.

In the particular case of ultra-luminous infrared galaxies (ULIRGs), the nuclei are embedded in large quantities of gas and dust produced by merging processes and massive star formation. In these conditions, the visual extinctions can be as high as Av>1000 mag when the H_2 column densities exceed > 10^{24}cm^{-2} in very compact regions of only a few pc (e.g. Costagliola et al. 2015; Aalto et al. 2017). In these extremely obscured environs, even the millimetre (mm)/sub-mm emission can be significantly attenuated by self- or continuum absorption, thus probing only the gas emitted at distances ≥100 pc from the central engines (e.g. Aalto et al. 2015b; Martín et al. 2016). Complementing mm/sub-mm observations with radiatively pumped molecular lines emitted in the infrared (IR), where most of the ULIRGs luminosity is emitted, allows to probe deeper the regions of the dusty cores. In particular, H_2O lines are excited via absorption and re-emission of IR photons produced very close to the central engines, and therefore provide essential information about the physical conditions of the hidden power sources of ULIRGs.

Mrk 273 (F13428+5608) is a ULIRG ($L_{\rm IR} = 1.3\times10^{12} L_\odot$, Gao et al. 1999) located at a distance of 157 Mpc

($V_{\rm LSR}^{\rm optical}$=11339 km s^{-1}, z=0.037780, 1″=761 pc[1]). Its complex morphology reflects a recent merger event between two or more galaxies. Near-IR, radio emission, and HI images show two nuclei separated by ∼1″ in the northeast-southwest direction (hereafter the northern and southern nucleus) plus a weaker third source that might be another nucleus or a starburst region triggered by the merger (Majewski et al. 1992, Cole et al. 1999, Condon et al. 1991). The nature of the progenitors has been subject of several studies that claim either AGN or starburst activities. Mrk 273 is classified as a Seyfert 2 galaxy in the optical and near IR (U et al. 2013; Rodríguez Zaurín et al. 2014; Iwasawa et al. 2017), having an AGN bolometric luminosity of $\log(L_{\rm AGN})$=44.73 erg s^{-1}, and a ratio between the bolometric luminosity of the AGN and the total bolometric luminosity of the galaxy of $L_{\rm AGN}/L_{\rm Bol}$ = 0.08 (Nardini et al. 2009). Nevertheless, far infrared and millimetre data point to a compact ultraluminous starburst region in the northern nucleus (Condon et al. 1991, Majewski et al. 1992, Downes & Solomon 1998). The total star formation rate (SFR) of the galaxy is 139 $M_{\odot}$yr^{-1} (Cicone et al. 2014).

Molecular observations reveal a complex structure in the centre of Mrk 273. CO maps show extended gas streamers in the north-south direction, a nuclear disk (of 2″ size) oriented east-west, and a very compact core (0.35″ × 0.2″) containing a powerful starburst (Downes & Solomon 1998). All these components belong to the northern nucleus (which is the strongest radio source), while there is no evidence of significant amounts of molecular gas in the southern objects.

A cool molecular outflow has been detected in Mrk 273 using H_2, CO, and OH observations (U et al. 2013; Veilleux et al. 2013; Cicone et al. 2014; González-Alfonso et al. 2017). From CO (1 − 0) observations, the outflow appears clearly in both line wings at high velocities |v|>400 km s^{-1}, and extends from the northern nucleus about 600 pc to the north. The CO channel-velocity maps also show a low velocity component (v>150 km s^{-1}) of the red-shifted outflow expanding to the north. The total mass of the outflow estimated from CO is $\sim 2\times10^8 M_{\odot}$.

The multi-phase composition of the outflow has been revealed by infrared and optical observations. OH detections (Veilleux et al. 2013; González-Alfonso et al. 2017) probe a more compact and warmer phase of the outflow that expands at velocities (100-700 km s^{-1}). This component travels shorter distances (160 pc) before it presumably cools down, and its mass and mass-loss rate are $5\times10^7 M_{\odot}$ and $120 M_{\odot}$yr^{-1}. Colina et al. (1999) detected an ionised component of the outflow by using the [OIII] λ=5007Å optical line. The hot, ionised gas goes much further, as far as ±5″ (∼3.8 kpc) along the north-south direction, and reaches velocities as high as ±1200 km s^{-1}. Other IR and optical lines, namely H_2, HeI, Brγ, and [CII], also show the low velocity component of the outflow (±200 km s^{-1}), as well as a moderate velocity component (600±300) km s^{-1} heading towards the north (U et al. 2013; Janssen et al. 2016).

Despite being one of the most luminous ULIRGs in the local universe, molecular detections towards Mrk 273 were still scarce and limited to CO, OH, and H_2. In this paper we present observations of molecules detected for the first time in this galaxy in the mm/sub-mm and far-IR ranges. In Sect. 2 we present our observations with the NOEMA and *Herschel* telescopes and the data reduction. The continuum and spectroscopic data analyses are presented in Sect. 3, where we also describe our modelling of H_2O. The asymmetric, double-peaked line profiles of the inner disk are discussed in Sect. 4.1. The detection of the Mrk 273 outflow and its properties are presented in Sect. 4.2. A brief discussion of the expansion of the galaxy core can be found in Sect. 4.3. The non-detection of vibrationally excited HCN and HC_3N emission is addressed in Sect. 4.4. We also discuss the HCN/HNC, HCN/HCO^+, and HCO^+/HOC^+ brightness temperature ratios (Sect. 4.5). The different origin of HOC^+, the only species not peaking at the very centre, is discussed in Sect. 4.6. Finally, our conclusions are summarised in Sect. 5.

2. Observations and data reduction

2.1. NOEMA

The HCN, HCO^+, HNC (1 − 0) and HC_3N (10 − 9) lines were observed simultaneously with the NOEMA interferometer on April 7th, 2015 (with seven antennae), and June 12th and 15th, 2017 (with eight antennae during a total time of 8.9 hours (precipitable water vapour (pwv)∼5-9 mm), while the HCN, HCO^+ and HOC^+(3 − 2) transitions were observed, also simultaneously, for 5.6 hours (pwv∼1-2 mm). The receivers were tuned to centre their lower side bands at 85.8 GHz (λ ∼3 mm) and 257.5 GHz (λ ∼1 mm) respectively. The receivers were connected to the WideX correlator and provided a 3.6 GHz bandwidth in two orthogonal polarisations (which were averaged). The data were calibrated and imaged with CLIC and MAPPING within the GILDAS′ package[2]. 3C84 was used as a bandpass calibrator, and the phase and flux calibrations were done by observing 1418+546 and MWC349 respectively.

The observations were centred on RA (J2000) = 13$^{\rm h}$:44$^{\rm m}$:42$^{\rm s}$.1 , DEC (J2000) = 55°:53′:13″.5. The original spectral resolutions of 6.8 km s^{-1} (3 mm) and 2.3 km s^{-1} (1 mm) were smoothed to 68-70 km s^{-1}. The final rms of the cubes, averaged across the spectral channels that do not contain line emission, are 0.3 mJy beam^{-1} (3 mm) and 1.3 mJy beam^{-1} (1 mm). We used a natural weighting mode and 0″.8 (for the 3 mm data) and 0″.05 (for the 1.3 mm data) pixel sizes to create the data cubes, and the Hogbom deconvolution method to clean them. The size of the primary beams were 58″.6 and 19″.6, and the angular resolutions achieved were (4″.9 × 4″.5) and (0″.61 × 0″.55) with position angles (P.A.) of -80° and +34° for the 3 mm and 1 mm transitions respectively. At the adopted distance of Mrk 273, these resolutions correspond to (3.7 × 3.4) kpc and (460 × 420) pc spatial scales.

None of our observed lines were previously detected in Mrk 273. Therefore, a comparison with single-dish data to estimate the missing flux is not possible. However, given the NOEMA configurations used, the maximum recoverable scales for our 1 mm and 3 mm observations are 2″.5 and 17″ respectively, which are well above (about one order of magnitude) the emission sizes of the molecules (see Sect. 3.3.1 and Table 3). Hence, we can safely claim that there was no flux filtered out in our observations.

2.2. Herschel

The H_2O data were taken with the Photodetector Array Camera and Spectrometer -PACS (Ott 2010; Poglitsch et al. 2010) and the Spectral and Photometric Imaging Receiver -SPIRE (Griffin et al. 2010) on December 16, 2012 and November 21, 2010 respectively. The absorption water lines observed with Herschel/PACS are new detections in Mrk 273, while the emission transitions detected with Herschel/SPIRE were already reported

[1] https://ned.ipac.caltech.edu

[2] http://www.iram.fr/IRAMFR/GILDAS

by Lu et al. (2017). The PACS observations[3] (PI: González-Alfonso) were performed in high spectral sampling range spectroscopy mode in first and second orders of the grating, resulting in a velocity resolution of ~ 170 – 265 km s^{-1}. The spectra were reduced with the standard product generation pipeline version 14.2.0. The nuclear far-IR emission from Mrk 273 was unresolved with the PACS 5spaxel×5spaxel IFU with 9.″4 x 9.″4 spaxels, so the spectra were extracted using the point source correction task available in the *Herschel* interactive processing environment -HIPE (Ott 2010) version 14.0.1. The spectra were then scaled to the integrated flux level of the central 3 × 3 PACS spaxels to compensate for pointing offsets and jitter which act to move flux out of the central spaxel. The H_2O spectra were sampled in velocities of 20-40 km s^{-1} per channel width. Polynomial baselines of orders <3 were then removed, and the final rms are 0.2-0.3 Jy km s^{-1}. The lines were fitted with Gaussian line profiles using the GILDAS software CLASS (Fig. 3).

The SPIRE observation[4] (PI: P. P. van der Werf) was conducted using a single pointing centred on Mrk 273 in high spectral resolution, sparse image sampling mode with a resolution of 1.2 GHz (~250-360 km s^{-1}) in the two observing bands (447 – 989 GHz and 958 – 1545 GHz). In total, 99 repetitions (198 FTS scans) were performed for a total on source time of 13187 s. The data reduction was done with the standard single pointing pipeline available in HIPE version 14.0.1 and a bootstrap method was used to extract the line fluxes. The individual scans were averaged together and a polynomial baseline was extracted from each detector before all lines were fitted simultaneously using Gaussian profiles convolved with a sinc function (Fig. 4). After 1000 repetitions of this procedure, Gaussians were fitted to the resulting flux distribution of each line to get the mean line flux together with its standard deviation.

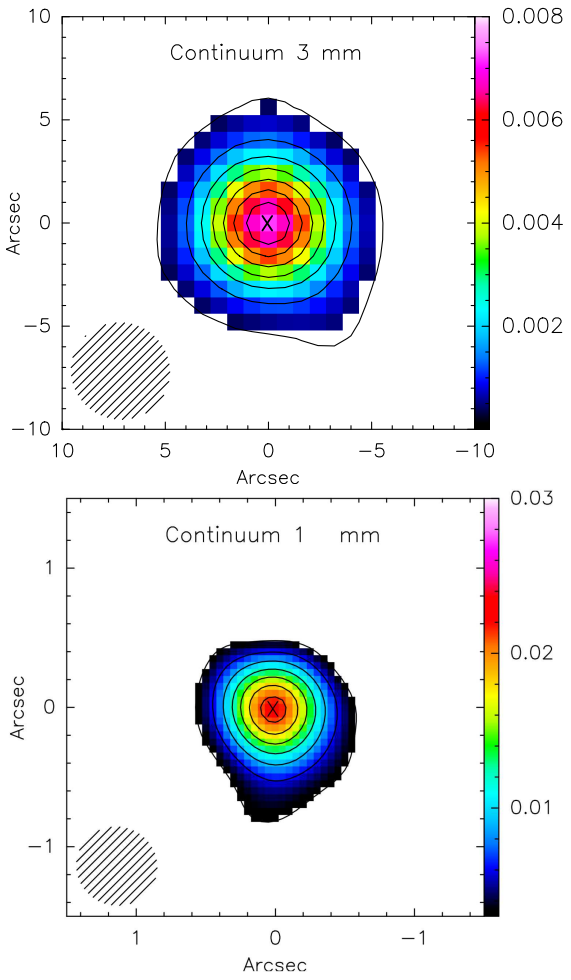

Fig. 1: Continuum maps at 3 mm and 1 mm. Contour levels start at a significance of 5σ with respect to the rms measured in both images (rms = 0.07 mJy channel^{-1} and 0.6 mJy channel^{-1} for the 3 mm and 1 mm maps respectively). The contour steps are 1 and 3 mJy km s^{-1} beam^{-1}. The crosses at the centres mark the continuum peaks, which we take as the location of the northern nuclear source (see Sect. 1). The synthesised beams are shown in the bottom left corner. The colour flux scales are in Jy km s^{-1} beam^{-1}.

3. Results

3.1. Continuum

We first created the 3 mm (~89 GHz) continuum visibilities including only the channels free of line emission after smoothing to the final spectral resolution. These visibilities were then subtracted from the total emission in the uv plane. Using the task *uv_fit* within the MAPPING package, we measured the size and flux of the 3 mm continuum. Our values were calculated by fitting an elliptical Gaussian in the Fourier plane. Circular and elliptical fits gave consistent values within the errors. Given that the images of the continuum and line emissions are quite round, but not entirely, we opted for using elliptical fits in order to take into account small asymmetries in the emission. We measured a spatially-integrated flux density of the 3 mm continuum of 8.24 ± 0.07 mJy and a deconvolved size of (1.92 ± 0.06)″ × (1.83 ± 0.07)″ with a P.A.=(−90 ± 30)°. This is similar to the 111 GHz continuum flux density of 11±2 mJy obtained by Downes & Solomon (1998).

Due to the very broad line widths at zero intensity (500-1100 km s^{-1}) in the 1 mm band (~265 GHz) and the narrow bandwidth of the correlator, almost all channels contain line emission. Therefore, the continuum visibilities were created using only nine line emission-free channels (15% of the total number of channels) at both edges of the spectrum. Including more channels could potentially lead to an overestimation of the continuum flux. A fit of an elliptical Gaussian in the uv plane gives an integrated flux of 28.6 ± 0.9 mJy, with a deconvolved size (FWHM -full with at half maximum- of the Gaussian) of (0.36 ± 0.03)″ × (0.27 ± 0.03)″ ~(270×200 pc) with a position angle of (24 ± 12)°. The integrated intensities of the continuum at 1 mm and 3 mm are plotted in Fig. 1.

3.2. Line profiles

3.2.1. Nuclear emission

Figure 2 shows the spectra of all observed lines with NOEMA extracted from the whole region (top panels), and from the central pixel of the observations (bottom panels). The total emission was integrated using masks in the moment zero maps of the HCO$^+$(1 – 0) and (3 – 2) lines, which show the most extended emission at 1 mm and 3 mm (Table 3). These masks were also used to integrate the emission of the more compact species observed at similar frequencies (i.e. one mask over HCO$^+$(1−0) for all 3 mm species, and other mask over HCO$^+$(3 – 2) for all 1 mm

[3] OBSIDs:1342257290-1342257294
[4] OBSID:1342209850

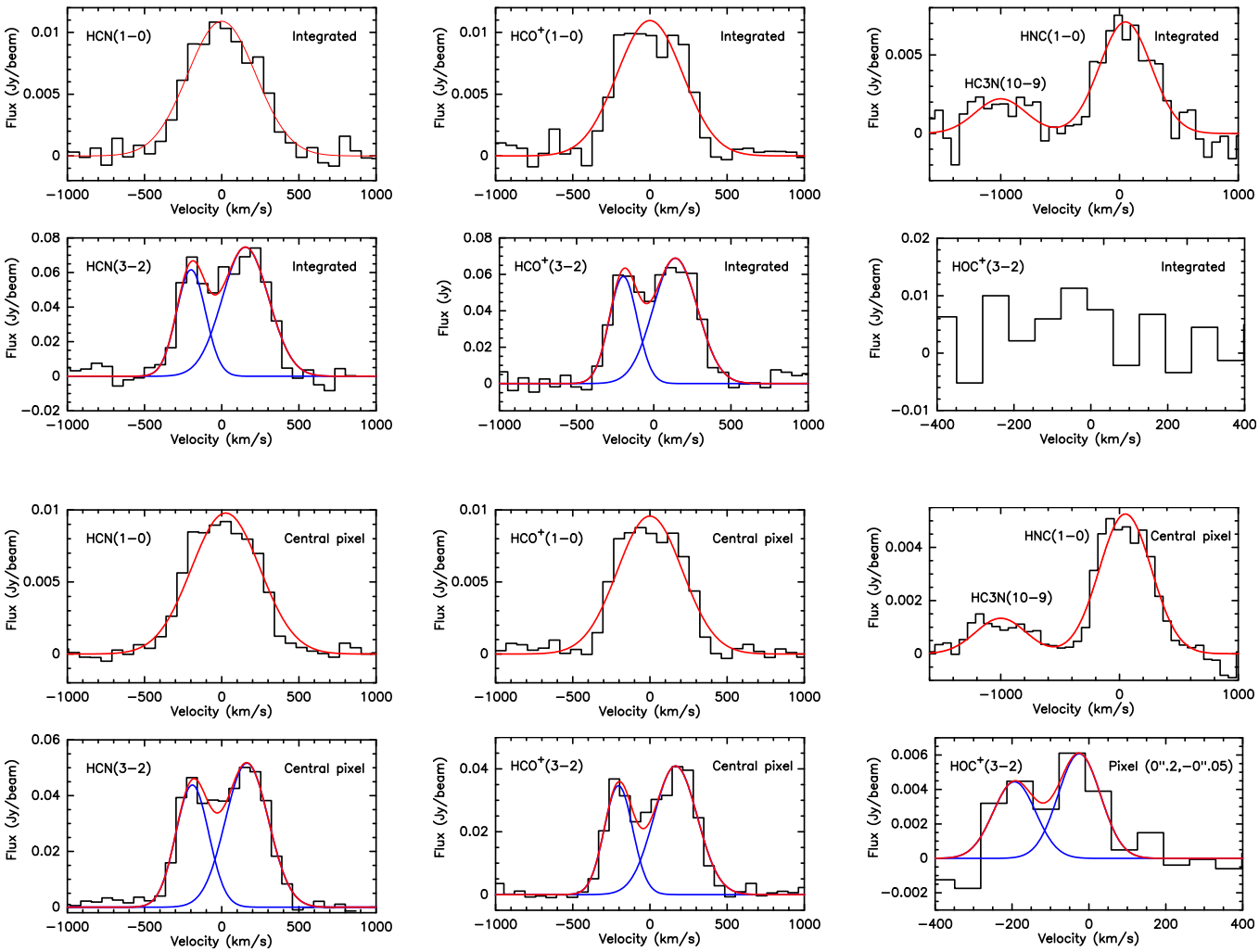

Fig. 2: Emission lines detected with NOEMA (black histograms) and Gaussian fits (total: red lines; if two components are present, individual components are displayed in blue colour). The velocity resolution is 68 km s^{-1} in all cases. The labels in the top right corners indicate if the spectra were extracted from the integrated emission ("Integrated", top panels), from the central pixel (bottom panels), or in the case of HOC$^+$, from the pixel at (0.″2, −0.″05).

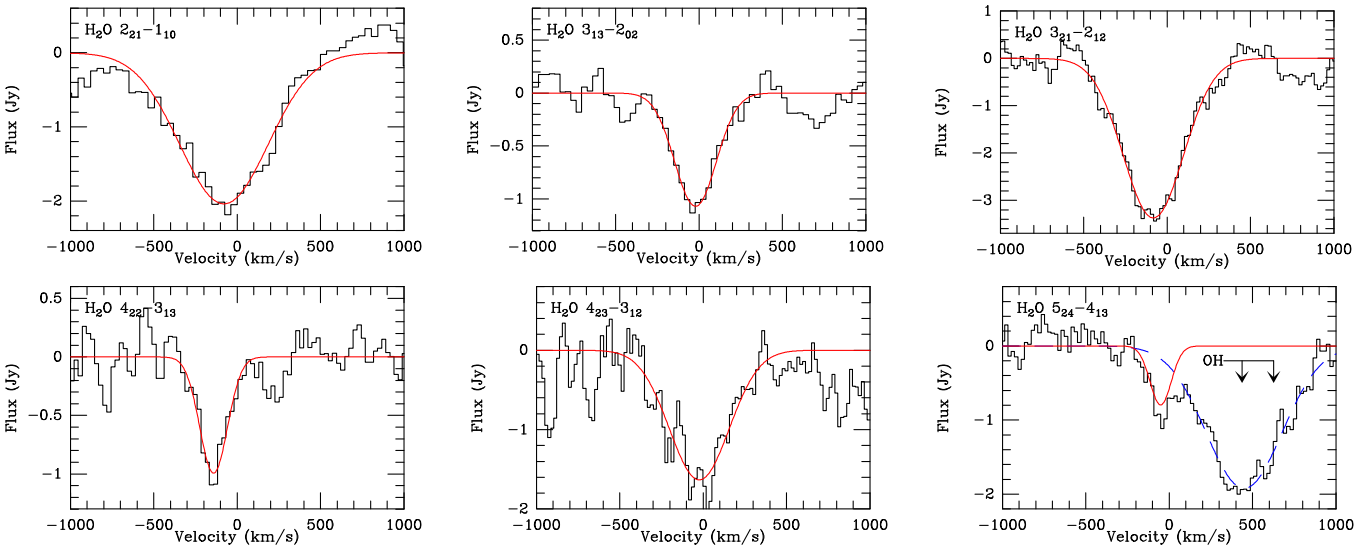

Fig. 3: H_2O absorption lines (black histograms) detected with *Herschel*/PACS and Gaussian fits (red lines). The velocity sampling is 20-40 km s^{-1}.

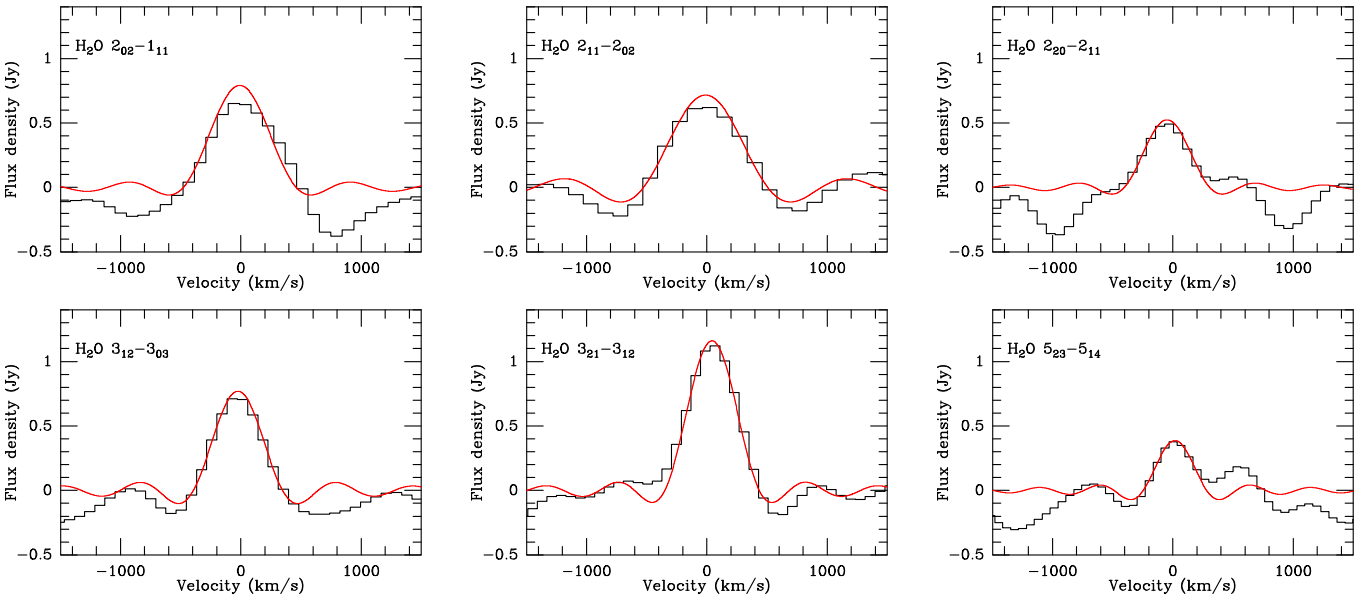

Fig. 4: H_2O lines (black histograms) detected with *Herschel*/SPIRE, and Gaussians fits (convolved with sinc functions).

species). While $HOC^+(1-0)$ is not detected, the $(3-2)$ transition is seen arising from a very compact region near the nucleus. When integrating the overall flux of the map, the emission of the $HOC^+(3-2)$ line drops below the noise and, thus, for comparison with the other molecules, we measure its flux in the pixel where it peaks (see Sect.3.3 for details). There, $HOC^+(3-2)$ is detected with a signal-to-noise ratio (SNR) of seven. Additionally, its central velocity is blue-shifted compared to the other lines observed with NOEMA (Table 1).

The 3 mm lines (HCN, HCO^+, HNC and $HOC^+(1-0)$, and $HC_3N(10-9)$) have roughly Gaussian-like profiles, although their peaks are slightly flat-topped. These lines were fitted with single Gaussian velocity profiles (Fig. 2). On the other hand, the 1 mm lines (HCN, HCO^+ and $HOC^+(3-2)$) are double-peaked. To account for these profiles, we fitted two Gaussians (their parameters are listed in Table 1). The intensity of the dip between the double peaks is 19 mJy and 26 mJy for the HCN and $HCO^+(3-2)$ lines respectively. The dip appears at slightly blue-shifted velocities, specifically at -30 km s^{-1} for $HCO^+(3-2)$, and -60 km s^{-1} for $HCN(3-2)$. The nature of these double-peaked profiles is further discussed in Sect. 4.1.

Figures 3 and 4 show the H_2O line profiles observed with *Herschel* PACS and SPIRE and the best Gaussians fits. All transitions were fitted by single Gaussian profiles (for the SPIRE lines, the Gaussians were convolved with a sinc function, Sect. 2.2). $H_2O\,(5_{24}-4_{13})$ is partially blended with an OH line at 71μm. To disentangle the emission of the two species, we fitted a double Gaussian profile to the observed spectrum.

It is important to note that all Gaussian fits to the water lines observed with PACS are blue-shifted to velocities between -20 km s^{-1} and -140 km s^{-1} (Table 2). Interestingly, these values are, to within the errors, the same as the velocities of the dips in the profiles of HCO^+ and $HCN(3-2)$. The connection between the two is discussed in Sect. 4.1.

3.2.2. High velocity emission

None of the 3 mm and far-IR water lines show obvious extended line wings, which would reveal the Mrk 273 molecular outflow previously detected with CO, OH, and H_2 by U

Table 1: Gaussian fit parameters to the emission lines detected with NOEMA.

	Flux [Jy km s^{-1}] *	Line peak [mJy] *	FWHM [km s^{-1}]	Central velocity [km s^{-1}]	Pixel
HCN (1 − 0)	6.0 ± 0.9	10.9	520 ± 85	0 ± 0	All
HCO$^+$(1 − 0)	5.8 ± 0.8	11.0	501 ± 78	0 ± 0	All
HNC (1 − 0)	3.9 ± 0.4	7.1	517 ± 59	50 ± 0	All
HC$_3$N (10 − 9)	1.2 ± 0.3	2.2	500 ± 0	0 ± 0	All
HCN (1 − 0)	5.4 ± 0.8	9.8	524 ± 79	26 ± 0	(0″, 0″)
HCO$^+$(1 − 0)	5.0 ± 0.7	9.6	495 ± 78	0 ± 0	(0″, 0″)
HNC (1 − 0)	2.9 ± 0.3	5.2	516 ± 51	50 ± 0	(0″, 0″)
HC$_3$N (10 − 9)	0.7 ± 0.2	1.3	500 ± 0	0 ± 0	(0″, 0″)
HCN (3 − 2)$_1$	14.9 ± 0.8	63.3	220 ± 179	−198 ± 71	All
HCN (3 − 2)$_2$	28.8 ± 0.5	76.6	354 ± 170	154 ± 83	All
HCO$^+$(3 − 2)$_1$	13.3 ± 0.7	58.7	213 ± 136	−197 ± 66	All
HCO$^+$(3 − 2)$_2$	24.7 ± 4.2	68.7	338 ± 159	140 ± 75	All
HCN (3 − 2)$_1$	11.7 ± 0.6	43.8	251 ± 130	−190 ± 63	(0″, 0″)
HCN (3 − 2)$_2$	18.0 ± 0.1	51.7	328 ± 134	164 ± 63	(0″, 0″)
HCO$^+$(3 − 2)$_1$	8.0 ± 1.0	34.6	216 ± 0	−203 ± 92	(0″, 0″)
HCO$^+$(3 − 2)$_2$	14.4 ± 0.6	40.9	331 ± 199	166 ± 89	(0″, 0″)
HOC$^+$(3 − 2)$_1$	0.6 ± 0.3	4.4	130 ± 0	−197 ± 0	(0.2″,-0.05″)
HOC$^+$(3 − 2)$_2$	1.0 ± 0.2	7.6	130 ± 0	−27 ± 0	(0.2″,-0.05″)

Notes: The last column indicates whether the spectra were extracted from only one pixel, or from all pixels showing significant emission. *: The units of flux and line peak estimated in a single pixel are Jy km s^{-1} beam^{-1} and mJy beam^{-1} respectively. For the $(J - J')$=(3 − 2) lines near λ=1 mm, we denote the two Gaussian components with the subscripts "1", and "2". Parameters with zero errors were fixed.

Table 2: Gaussian fit parameters to the water lines detected with *Herschel*.

	$\lambda_{\rm rest}$ [μm]	$E_{\rm low}$ / $E_{\rm upper}$* [K]	Flux [Jy km s^{-1}]	Line peak [mJy]	FWHM [km s^{-1}]	Central velocity [km s^{-1}]
H$_2$O ($2_{2,1} - 1_{1,0}$)	108.073	61	−1356 ± 87	−2.0 ± 0.1	625 ± 48	−79 ± 21
H$_2$O ($3_{1,3} - 2_{0,2}$)	138.528	101	−334 ± 46	−1.1 ± 0.1	294 ± 49	−21 ± 20
H$_2$O ($3_{2,1} - 2_{1,2}$)	75.381	114	−1531 ± 60	−3.4 ± 0.2	427 ± 19	−82 ± 8
H$_2$O ($4_{2,2} - 3_{1,3}$)	57.636	205	−240 ± 62	−1.0 ± 0.1	215 ± 70	−140 ± 26
H$_2$O ($4_{2,3} - 3_{1,2}$)	78.742	275	−733 ± 138	−1.6 ± 0.2	422 ± 94	−23 ± 38
H$_2$O ($5_{2,4} - 4_{1,3}$)	71.067	396	−127 ± 28	−0.8 ± 0.1	150 ± 35	−51 ± 14
H$_2$O ($2_{0,2} - 1_{1,1}$)	303.456	101	421 ± 74	0.8 ± 0.1	207 ± 41	−24 ± 75 *
H$_2$O ($2_{1,1} - 2_{0,2}$)	398.643	137	408 ± 42	0.71 ± 0.06	164 ± 40	−26 ± 32 *
H$_2$O ($2_{2,0} - 2_{1,1}$)	243.974	196	220 ± 67	0.5 ± 0.1	148 ± 75	−63 ± 56 *
H$_2$O ($3_{1,2} - 3_{0,3}$)	273.193	249	223 ± 52	0.8 ± 0.1	137 ± 38	−39 ± 38 *
H$_2$O ($3_{2,1} - 3_{1,2}$)	257.795	305	545 ± 62	1.2 ± 0.1	171 ± 3	28 ± 25 *
H$_2$O ($5_{2,3} - 5_{1,4}$)	212.526	642	128 ± 43	0.4 ± 0.1	65 ± 51	3 ± 54 *

Notes: Some lines are affected by strong noise that increases the errors in the Gaussian fittings. * The first six H$_2$O lines were detected in absorption with PACS, and we show the energy of their lower level. The last six lines were detected with SPIRE in emission, so we show the energy of their upper level. * Due to the low velocity resolution of the SPIRE instrument ∼250-360 km s^{-1}, these values are very uncertain and we do not consider them in our discussion.

et al. (2013), Veilleux et al. (2013), Cicone et al. (2014), and González-Alfonso et al. (2017). For the 1 mm observations, the spectrum of the overall integrated emission has no evident signatures of line wings either. However, in the central pixel the HCN profile exhibits a line wing that extends between -400 and ∼1000 km s^{-1}, while the red side shows no wing (Fig. 5). This emission is detected with an SNR∼5.

We used the JPL catalog (Pickett et al. 1998) to look for lines arising from 266.2 to 266.9 GHz, which correspond to the velocity range [-350,-1200] km s^{-1} where the HCN(3 − 2) wing-like feature is seen. CH_2NH ($4_{1,3} - 3_{1,2}$) is the most likely line arising at these frequencies, with an energy level of $E_{\rm low}$=19 K. This transition was detected in the LIRGs IC 860 and Zw 49-57, where its flux density is 3-4 times fainter than HCN(3 − 2) (Aalto et al. 2015b). Assuming a similar ratio and excitation conditions in Mrk 273, then CH_2NH would have a peak flux between 4.5 and 6 mJy, i.e. brighter than the emission we see. The HCN shoulder does not have a (single or double) Gaussian profile similar to the detected lines, but has the shape of a line wing. For these reasons, it seems unlikely that the emission comes from the CH_2NH line, although a potential contamination cannot be ruled out.

The two nuclei of Arp 220 have HCN (3 − 2) and (4 − 3) blue-shifted wings very similar to what we observe here in Mrk 273

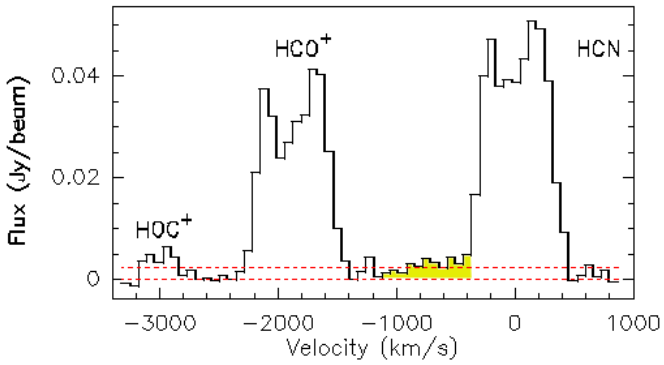

Fig. 5: Spectrum of the central pixel for the $(J - J')$=(3 − 2) lines of HCN, HCO^+ and HOC^+. The baseline of order 0 and the 3 × rms flux (calculated at the final velocity resolution of 68 km s^{-1}) are marked with horizontal dashed lines. The outflow emission at the blue-shifted velocities of HCN is highlighted in yellow.

(Martín et al. 2016). The fact that these bumps appear in both HCN transitions, while there is no corresponding CH_2NH line close to the HCN(4 − 3) frequency, strengthens our claim that the line wing in Mrk 273 comes from HCN(3 − 2), and that it is tracing gas outflowing at high velocities. In summary, given the feature intensity, spectral shape, and integrated emission (see next section), we conclude that the HCN(3 − 2) blue-shifted shoulder comes from the outflowing gas moving at approximate velocities between -400 and -1000 km s^{-1}. In Sects. 3.3.2 and 4.2 we discuss in more detail the properties of this molecular outflow.

3.3. Moment maps of HCN, HCO^+, HNC and HOC^+

3.3.1. Position and size of the nuclear emission

Figure 6 and Table 1 show the integrated intensities of the HCN, HCO^+, HNC and HOC^+ lines. The deconvolved emission sizes and position angles of all lines were measured in the uv plane by fitting elliptical Gaussians with the task *uv_fit* within MAPPING, and are listed in Table 3. The continuum and the HCN, HCO^+, and HNC lines have their peak intensities at the central pixel, which we take as the location of the northern nuclear source. On the contrary, the HOC^+ maximum is found at an offset (0.″2, −0.″05), corresponding to (152, −38) pc to the southeast. The position accuracy of our observations can be calculated from:

$$\Delta\alpha, \Delta\delta \simeq 0.6 \times (SNR)^{-1} \times \theta_b, \quad (1)$$

where $\Delta\alpha, \Delta\delta$ are the errors in RA and DEC, and θ_b is the synthesised beam size (Condon 1997; Ivison et al. 2007). For HOC^+(3 − 2), we have a $\Delta\alpha, \Delta\delta \simeq 0.''1$ (∼80 pc), confirming our claim that its shift is real, at least in RA (because the HOC^+ offset in declination is smaller than our position accuracy). In Sect. 4.6, we further discuss the origin of HOC^+.

Downes & Solomon (1998) estimated a CO (1 − 0) emission deconvolved size of (0.″9 × 0.″6) with a beam of (1.″4 × 1.″3). We obtain larger sizes for the HCN, and HCO^+(1 − 0) lines (∼ (2″ × 2″) equivalent to ∼1.5 kpc, Table 3), most probably because we collect more emission within our larger beam of (4.″9 × 4.″5). In the following we refer to this region as the outer disk. The HCN and HCO^+(3 − 2) lines, however, are confined to a much smaller region of (0.″4 × 0.″3) (∼(300×230) pc, Table 3), implying that the denser, star-forming gas is more concentrated in the nucleus. We refer to this as the inner disk. Despite our high angular resolution at 267 GHz, the nucleus is still unresolved and does not show any structures in the moment zero maps, implying a very compact core that do not expand more than < 0.″3 (230 pc). Indeed, from our H_2O modelling we estimate the size of the core as ∼50 pc (see Sect. 3.4 for details).

HC_3N (10 − 9) and HOC^+(3 − 2) are faint (although we detect the latter with an SNR of ∼7 in the pixel where it peaks) and unresolved at our resolution. Therefore, we cannot measure their emission sizes.

3.3.2. Integrated intensity of the outflow

The moment zero map of the outflow traced by HCN(3−2) (highlighted in yellow in Fig. 5) is shown in Fig. 7. After centering the spectrum at the HCN(3 − 2) rest frequency, we integrated the emission of all pixels in the velocity range [-1100, -400] km s^{-1}. Its morphology is composed of two main peaks of emission; a stronger one with an elliptical shape around the centre, and a fainter and rounder feature at ∼0.8″ (∼600 pc) to the north. In the central pixel, the peak flux has an SNR of ∼5 (measured at the final velocity resolution), while the integrated flux density measured in the moment zero map is 2.4 Jy km s^{-1}.

We measured the size of the outflow by fitting two ellipses to the main peaks seen in the moment zero map (see Fig. 7). We take the size of the outflow as the projected distance between the central pixel and the centre of the northern ellipse. We measure a size of 0.″61 ± 0.″05, equivalent to 464 pc, with a position angle of 10 ± 3°. The direction of the flow, heading to the north, is consistent with the outflowing gas detected with CO (1 − 0) by Cicone et al. (2014).

3.3.3. Velocity fields and position-velocity maps

Figures 8 and 9 show the velocity fields and position-velocity (p-v) maps of HCN, HCO^+ and HNC. The velocity fields reveal the rotation of the Mrk 273 nuclear disk (see Downes & Solomon (1998) for a detailed study of the disk properties). There are significant differences in the morphologies of the iso-velocity contours of the various observed lines. HCN and HCO^+(1 − 0) trace rotating gas in the outer disk showing a south-east to north-west direction. However, the less extended gas traced by HNC (1 − 0) shows a north-east to south-west rotation, similar to the gas in the inner disk traced by the HCN (3 − 2) and HCO^+(3 − 2) lines. The rotation in the central < 0.″5 follows the velocity fields traced by the warm, and also compact, gas traced by H_2, Brγ and [FeII] (Medling et al. 2014; U et al. 2013). This is consistent with the two kinematic systems of the disk already discovered by Downes & Solomon (1998) by using the CO (1 − 0) and CO (2 − 1) lines with beam sizes (1.″4, 1.″3) and (0.″6, 0.″6). The agreement between the Downes & Solomon (1998) velocity fields and ours, despite the difference in angular resolution, suggests that this effect is not due to the larger beam size of our 3 mm data. .

Figure 9 shows the p-v diagrams of the HCN and HCO^+ lines along cuts through the centre and perpendicular to the axes of rotation as plotted with dashed lines in Fig. 8. The outer disk traced by the (1 − 0) lines shows maximum velocities ± 300km s^{-1}, though most of the gas exhibits velocities within the smaller range of ± 150km s^{-1}. The p-v diagrams of HCN and HCO^+(3 − 2) show that the gas in the inner disk rotates faster, reaching maximum velocities of ± 400 km s^{-1}, although the av-

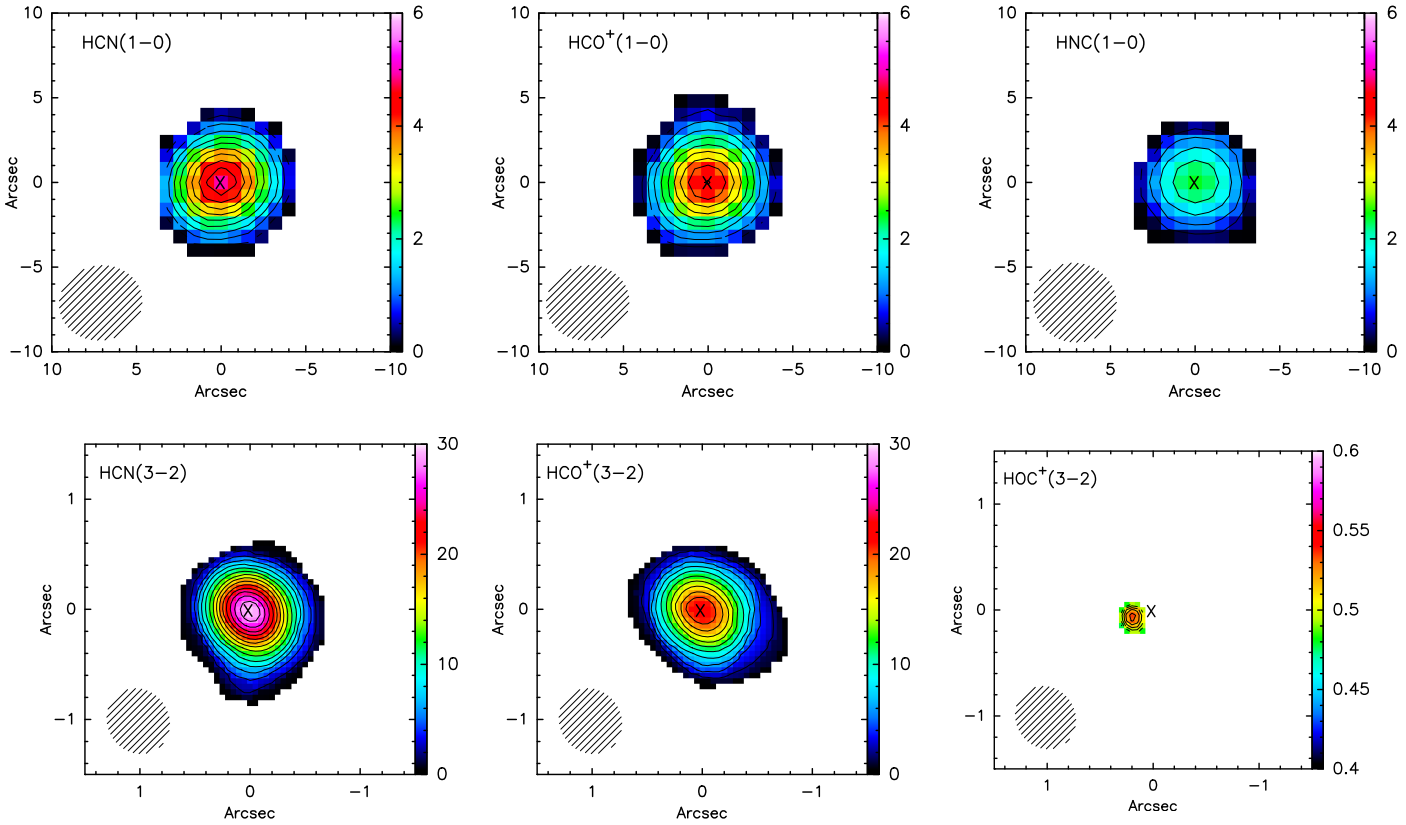

Fig. 6: Integrated intensities (moment zero maps). Contour levels for HCN, HCO^+ and HNC $(1-0)$ go from 0 to 6 Jy kms^{-1}beam^{-1} with a step of 0.5 Jy kms^{-1}beam^{-1}. For HCN $(3-2)$ and $HCO^+(3-2)$ the levels range from 2 to 30 Jy kms^{-1}beam^{-1} with a step of 2 Jy kms^{-1}beam^{-1}. For $HOC^+(3-2)$, the contours are from 0.4 to 0.6 Jy kms^{-1}beam^{-1} with a step of 0.04 Jy kms^{-1}beam^{-1}. Note the different scales between the $(1-0)$ and the $(3-2)$ lines. The crosses in the centre of each panel indicate the location of the nuclear source. The synthesised beam is shown in the bottom-left corner of each panel. North is up, and east is to the left.

Table 3: Global properties of the lines detected with NOEMA.

	$\nu_{\rm rest}$ [MHz]	K Jy^{-1}	Size^a [″]	P.A.^{a} [°]	L′ [K km s^{-1} pc^2]
HCN $(1-0)$	88631.8	7.1675	$(2.0\pm0.2)\times(1.6\pm0.2)$	-39 ± 20	2.5×10^8
$HCO^+(1-0)$	89188.6	7.0783	$(2.2\pm0.2)\times(1.7\pm0.2)$	1 ± 16	2.8×10^8
HNC $(1-0)$	90663.6	6.4696	$(2.4\pm0.4)\times(2.0\pm0.3)$	-36 ± 35	2.2×10^8
HC_3N $(10-9)$	90979.0	6.4248	<1.6	—	—
HCN $(3-2)$	265886.4	51.4126	$(0.35\pm0.01)\times(0.31\pm0.01)$	68 ± 11	4.4×10^8
$HCO^+(3-2)$	267557.6	50.7724	$(0.40\pm0.01)\times(0.32\pm0.01)$	71 ± 5	2.6×10^8
$HOC^+(3-2)$	268451.1	50.4350	<0.3	—	—

Notes: ^{a} Calculated as the FWHM of the elliptical Gaussian fitted to the line emission in the uv-plane (see Sect. 3.3.1). The line luminosity is $L=\pi R^2 I$, where R is the source size in column four in parsec ($1''=761$ pc), and I is the integrated intensity (shown in Table 1) in units of K km s^{-1}.

erage speed is ±200 km s^{-1} at the edges of the disk, which are separated by $0\farcs2$ (~150 pc).

The dynamical mass of the inner, starbursting, disk, measured from the kinematics of the (3−2) lines, is $(4-5)\times10^9 M_\odot$, as calculated from RV^2_{rot}/G. Here $V_{\rm rot}$ is the average rotational velocity corrected for the 45 degree inclination of the disk (Downes & Solomon 1998), R is the size of the emission in pc (Table 3), and G is the gravitational constant.

3.3.4. Velocity dispersions

The velocity dispersions of the NOEMA data were calculated as

$$\sigma_v = \frac{FWHM}{2\times\sqrt{2\times ln(2)}} \quad (2)$$

The moment 2 maps of HCN, HCO^+ and HNC are shown in Fig. 10. All lines reach similar maximum dispersions of 500 km s^{-1}. We explored the Toomre (1964) stability criterion,

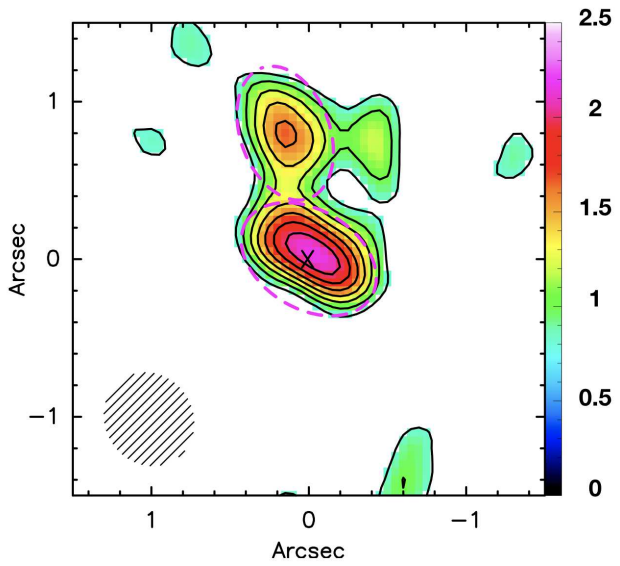

Fig. 7: Integrated intensity of the outflow seen in HCN (3 − 2) between -1100 km s^{-1} and -400 km s^{-1} (yellow region marked in Fig. 5). The cross in the centre marks the location of the nuclear source. The contours start with a 5σ flux and go from 0.8 mJy kms^{-1} beam^{-1} to 2.5 Jy kms^{-1} beam^{-1} with steps of 0.2 mJy kms^{-1} beam^{-1}. The magenta dashed ellipses show the regions fitted to the two main components. The synthesised beam is plotted in the bottom-left corner.

$Q \geq 1$, for the inner, starbursting, gaseous disk to check its stability against gravitational perturbations, as

$$Q = \frac{\sigma_v \times \kappa}{\pi \times G \times \Sigma} \quad (3)$$

where κ is the epicyclic frequency, G is the gravitational constant, and Σ is the surface density of the gas. The surface density in the inner 380 pc of Mrk273 is 37500 $M_{\odot}/pc^2$ (Yun & Scoville 1995). We note that this value was calculated in a region slightly larger than the radius of the inner disk (of ∼300 pc), but it is still a good approximation if compared to the size of the outer disk (1.5 kpc). For the epicyclic frequency, we assumed a Keplerian disk. Thus, $\kappa = \omega$, being ω the angular velocity. For consistency, we calculated ω in the same radius, of 380 pc, and used the average rotational velocities from our HCN and HCO$^+$(3 − 2) velocity maps (200 km s^{-1}, Figs. 8 and 9). We obtain $Q = 0.5$, which indicates that the inner disk is unstable and clumpy/turbulent enough to form further self-gravitating condensations of gas.

3.3.5. HCN and HCO$^+$ channel-velocity maps

Figures 11 to 14 show the channel maps of HCN and HCO$^+$(1 − 0) and (3 − 2) between -500 and +500 km s^{-1} in steps of 50 km s^{-1}, with a beginning intensity contour level of 5σ. The (1 − 0) lines show emission away of the nucleus in all directions. In particular, the HCN(1 − 0) channel map reveals gas in the northern direction as far as 10″ from the centre at negative velocities, as well as elongations towards the south at ±300 km s^{-1}. Some extensions to the east and south-east are also seen in some channels. The HCO$^+$(1 − 0) emission is similarly extended, but the structure towards the south is perhaps the most distinct (e.g. channels ± 150 km s^{-1}). Nevertheless, extensions to the north (± 200 km s^{-1} and ± 300 km s^{-1}), east (± 250 km s^{-1}) and west (+150 km s^{-1} and +250 km s^{-1}) are also seen.

The HCN and HCO$^+$(3 − 2) channel maps trace denser gas in the inner parts of the galactic disk (≤ 300 pc), although some emission can be seen in the central ±1″ (±800 pc), and their elongations are even more obvious than in the (1 − 0) channel maps. HCN shows clear signs of emission towards the north in most channels (best seen between -250 km s^{-1} and +250 km s^{-1}). On the other hand, the gas traced by HCO$^+$ is more extended towards the south (e.g. -200 km s^{-1} and +50 km s^{-1}).

The most significant extensions to the north (from the HCN maps) and to the south (from the HCO$^+$ maps) are signatures of outflowing gas, and are further discussed in Sect. 4.2.

3.4. Modelling of H_2O

We have used the library of H_2O models generated by González-Alfonso et al. (2014) to fit the H_2O emission and absorption observed in Mrk 273. The models assume spherical symmetry, are non-local, and include excitation by both the far-infrared field emitted by warm dust (which is mixed with the H_2O molecules) and collisions with H_2. The collisional rates were taken from Dubernet et al. (2009) and Daniel et al. (2011), and a gas-to-dust ratio of 100 was adopted (Wilson et al. 2008). The models assume uniform physical properties ($T_{\rm dust}$, $T_{\rm gas}$, gas and dust densities, H_2O abundance). The source is divided into a set of spherical shells where the statistical equilibrium level populations are calculated. We assume an H_2O ortho-to-para ratio of 3. Line broadening is simulated by including a micro-turbulent velocity ($V_{\rm turb}$), with no systemic motions.

The modelled line fluxes and continuum flux densities scale as $(R/D_{\rm L})^2$ where R is the source radius and D_L is the luminosity distance, so that they are easily scalable to the properties of any source. Following Falstad et al. (2017) and González-Alfonso et al. (2017), we have fit the line fluxes with a combination of N_C model components by minimising χ^2, with the radius R of each component the only free parameter that is varied. We required $N_C = 2$ components to fit properly the PACS and SPIRE H_2O fluxes simultaneously. Since the models also make specific predictions for the spectral energy distribution (SED) of each component, and since H_2O probes the galaxy far-IR emission responsible for its excitation and more specifically the transition from the mid to the far-IR (González-Alfonso et al. 2010, 2014), we also included in the fit the continuum flux densities at 30 and 60 μm.

Figure 15 compares the observed H_2O fluxes and SED with the results of our best model fit, and Table 4 lists the properties of the two model components (shown with blue and green colours in Fig. 15). The two components show very different behaviours relative to the H_2O absorption and emission. We require a very compact (effective radius $R \sim 50$ pc), very warm ($T_{\rm dust} \sim 95$ K), and very optically thick ($\tau_{100\mu m} \gtrsim 4$) component (referred to as the "core") to account for the observed PACS absorption in several lines (primarily the $3_{13} - 2_{02}$ line at 138 μm, the $4_{22} - 3_{13}$ line at 58 μm, the $4_{23} - 3_{12}$ line at 79 μm, and the $5_{24} - 4_{13}$ line at 71 μm) and also the SPIRE emission in the $5_{23} - 5_{14}$ line at 212 μm (although this line is only marginally detected at the 3σ level). However, the core component predicts negligible emission in most SPIRE lines (and even absorption in the $2_{20} - 2_{11}$ line), which indicates the presence of a more extended component ($R \sim 280$ pc), moderately warm ($T_{\rm dust} \sim 55$ K), and with

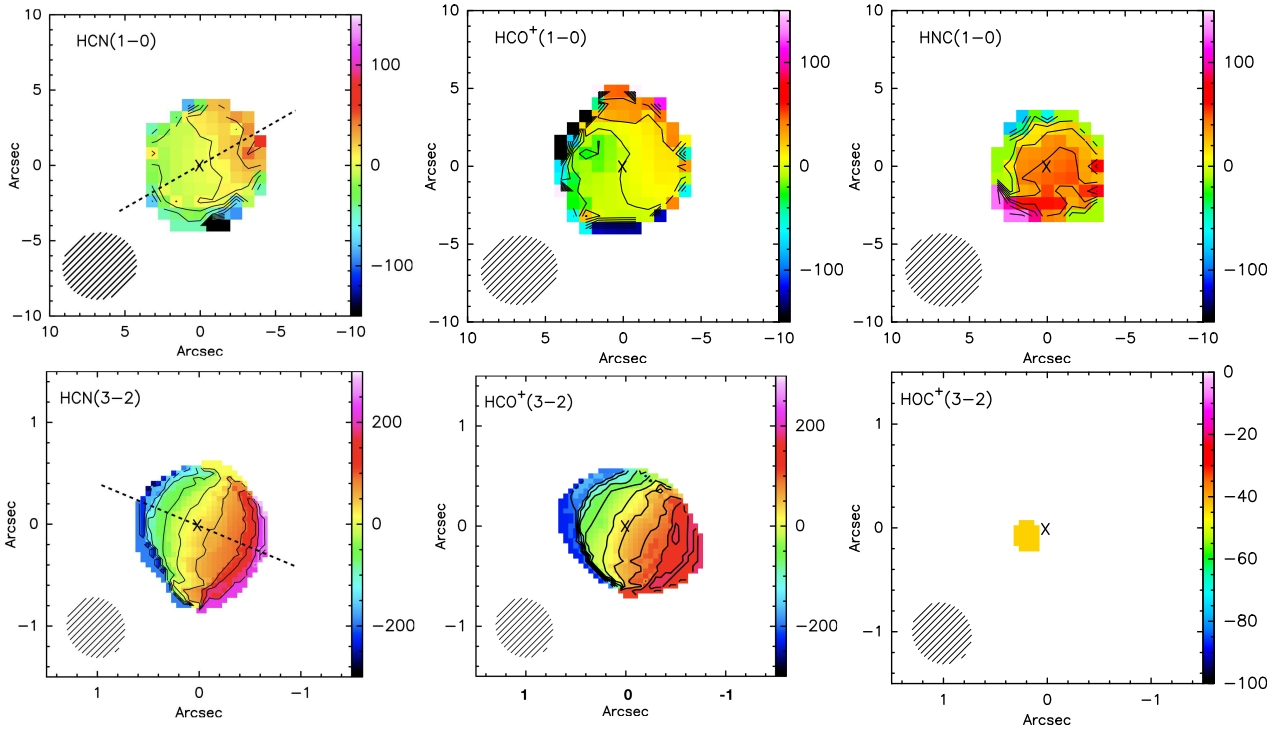

Fig. 8: Velocity fields (moment 1 maps). The coloured velocity scale (right axis) is in km s^{-1}. The step in contours is 20 kms^{-1} for all lines. Note the blue-shifted velocities of HOC$^+$(3 – 2). The crosses in the centre of each panel indicate the position of the nuclear source. The beam is shown in the lower left corner of each panel. North is up, and east is to the left. The dashed lines in the HCN plots indicate the cut for the p-v diagrams shown in Fig. 9.

Table 4: Results for the 2-component modelling of the H_2O lines in Mrk 273

Component	$T_{\rm dust}$ [K]	$\tau_{100\mu m}$	R [pc]	$L_{\rm IR}$ [10^{11} L$_\odot$]	$N(H_2O)$ [10^{16} cm^{-2}]	$X(H_2O)$ [10^{-6}]
Core	95 ($\gtrsim$ 80)	5.0 ($\gtrsim$ 4)	51 (40 – 60)	3.8 (2.3 – 5.0)	800 ($\gtrsim$ 400)	1.2 (0.6 – 3)
Inner disk	55 (45 – 65)	0.5 (0.2 – 1)	284 (180 – 360)	8.0 (6 – 12)	7.8 (5 – 20)	0.12 (0.08 – 0.5)

Notes: Numbers in parenthesis indicate the most plausible ranges, as inferred from all combinations with χ^2 not exceeding 1.7× the minimum value.

lower column ($\tau_{100\mu m} \sim 0.5$). This extended component, mostly responsible for the H_2O emission observed with SPIRE, is naturally identified with the inner disk traced by the $J = 3 - 2$ lines of HCO$^+$ and HCN (∼300 pc).

The two water components together provide a good fit to the far-IR emission, though the combined model underestimates, to some extent, the flux densities between 100 and 200 μm. This probably indicates a range in $T_{\rm dust}$ for the disk component, rather than a single value. It is also worth noting that the source luminosity is dominated by the disk (i.e. the starburst), with the core component accounting for $L_{\rm IR} \sim 4 \times 10^{11}$ L$_\odot$. The latter corresponds to ∼ 30% of the total IR luminosity, which is close to the estimated AGN contribution based on the 15−to−30 μm diagnostic (e.g. Veilleux et al. 2009). The blueshift of the absorption lines, which are dominated by the core component, is similar to that seen in the excited OH lines (González-Alfonso et al. 2017), suggesting that the core is expanding (more details in Sect. 4.3). Our model for the core also predicts significant emission at 265 GHz, ∼ 10 mJy, though this value is relatively uncertain because of its dependence on the actual continuum optical depth and the mass absorption coefficient of dust (κ_λ) at millimetre wavelengths[5].

4. Discusion

4.1. A rotating disk with continuum absorption

The integrated intensities, velocity fields and p-v diagrams of HCN and HCO$^+$ show the typical pattern of a rotating disk (Figs. 6, 8 & 9). Such a rotating body should in principle be reflected in the spectra as double-peaked lines. However, due to our relatively large beam size used to observe the (1 – 0) lines (4.″9 × 4.″5), most of the gas is concentrated in the central pixel and the velocity gradients within the beam are not well reproduced. Hence, our HCN and HCO$^+$(1 – 0) lines show a single Gaussian-like profile. On the other hand, the (3 – 2) transitions were observed with a resolution significantly higher

[5] For the core component, we modified the k_λ curve in Fig. 2 of González-Alfonso et al. (2014) in such a way that $\kappa_{1.3mm} = 0.9$ cm^2 g^{-1} of dust, more similar to the value used by Downes & Solomon (1998).

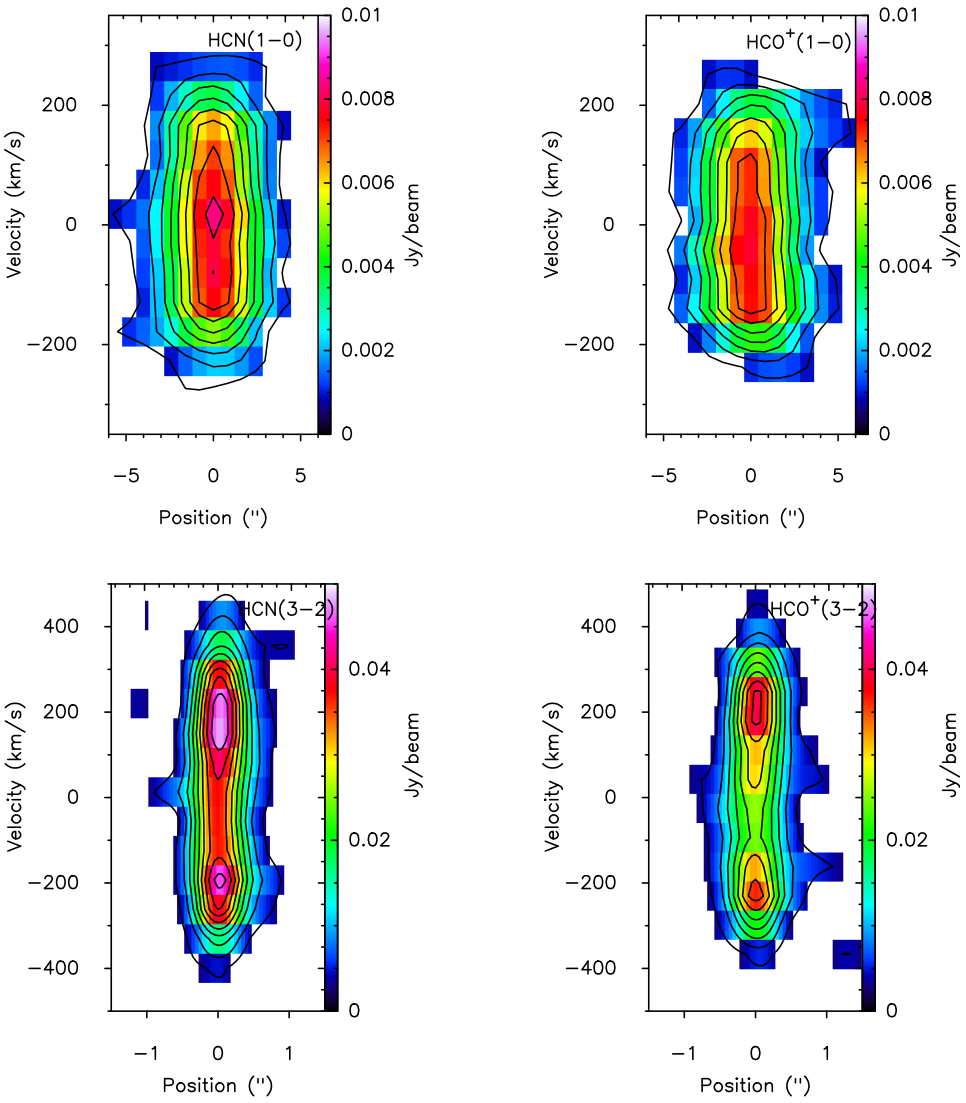

Fig. 9: Position-velocity (p-v) maps of HCN and HCO^+. The cuts along the axes of rotation are shown by the dashed lines in Fig. 8. Contour steps of the (1 – 0) maps go from 0.9 mJy beam^{-1} (3σ) to 7.9 mJy beam^{-1} with steps of 1 mJy beam^{-1}. For the (3 – 2) maps, contours go from 3.9 mJy beam^{-1} (3σ) to 59 mJy beam^{-1} with steps of 5 mJy beam^{-1}.

(0.″61 × 0.″55), so the velocity gradients are well traced and the spectral lines reveal the expected pattern of the inner rotating disk (see Sect. 3.3.1).

In addition, continuum absorption is also apparently contributing to the shape of the HCN and $HCO^+(3-2)$ profiles. Firstly, we note than the ∼20-25 mJy drop flux of the lines is very similar to the continuum flux density at these frequencies, of 29 mJy. Secondly, the velocity of the minimum flux, around -50 km s^{-1}, roughly coincides with the peak absorption velocities of the H_2O lines observed with PACS, and of the OH 84 μm and OH 65 μm lines presented in González-Alfonso et al. (2017). The foreground warm gas traced by H_2O and OH is absorbing the continuum (e.g. González-Alfonso et al. 2017), and the coincidence in velocities and continuum values of the dip in HCN and HCO^+ indicates that the dense gas might also be absorbing the background dust emission.

In this context, the two peaks of the HCN and $HCO^+(3-2)$ lines are probing the edges of the inner rotating disk, while the absorbed flux indicates the positions of the maximum column densities of the gas. The channel maps shown in Figs. 13 and 14 also show a minimum emission around -50 km s^{-1} and -100 km s^{-1} (better seen in the $HCO^+(3-2)$ map), the velocities at which there is a maximum absorption of the continuum.

Self-absorption might also be an extra factor affecting the line shapes if there is cooler foreground gas with high enough column densities. This, however, is difficult to disentangle from the continuum absorption in our data. In addition, it is possible that the opacity of the gas in the centre of Mrk 273 is high enough to result in flat-topped profiles such as some of those observed in the HCN and $HCO^+(1-0)$ transitions, even though these species are less abundant than CO. A hint of such a profile might be seen in the HCN, $HCO^+(1-0)$ transitions. We note that any kind of absorption implies that our estimations of line fluxes, luminosities, and molecules gas mass are lower limits to the actual values.

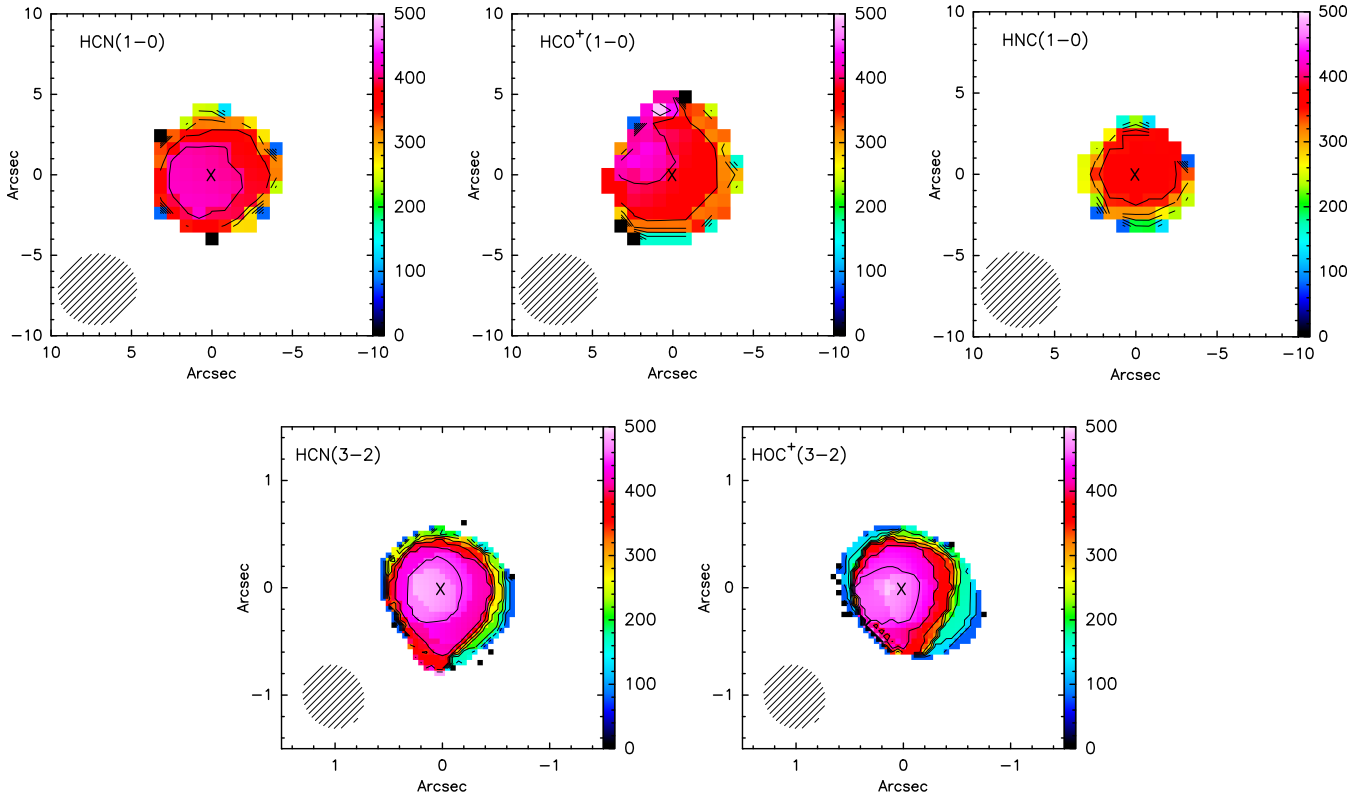

Fig. 10: Velocity dispersions. Contours go from 0 to 500 kms^{-1} with steps of 50 kms^{-1} for all lines. The crosses in the centre of each panel indicate the position of the nuclear source. The synthesised beam is shown in the bottom-left corner of each panel. North is up and East is to the left.

Table 5: Brightness temperature ratios in Mrk 273 (row/column), evaluated over the entire emission.

	HCN(1 − 0)	HCO$^+$(1 − 0)	HNC(1 − 0)	HC$_3$N(10 − 9)	HCN(3 − 2)	HCO$^+$(3 − 2)	HOC$^+$(3 − 2)†
HCN(1 − 0)	1.00±0.07	1.00±0.07	1.8±0.2	6±1	—	—	—
HCO$^+$(1 − 0)	1.00±0.07	1.00±0.07	1.8±0.2	6±1	—	—	—
HNC(1 − 0)	0.55±0.05	0.55±0.05	1.0±0.1	3.2±0.8	—	—	—
HC$_3$N(10 − 9)	0.17±0.04	0.17±0.04	0.31±0.08	1.0±0.3	—	—	—
HCN(3 − 2)	—	—	—	—	1.00±0.06	1.13±0.06	10±5
HCO$^+$(3 − 2)	—	—	—	—	0.88±0.05	1.00±0.06	9±4
HOC$^+$(3 − 2)†	—	—	—	—	0.10±0.05	0.11±0.06	1.0±0.7

Notes: Due to differences in the observed areas, we do not list the ratios between the 3 mm and 1 mm lines (see Sect. 4.5). † For HOC$^+$(3 − 2) we used the temperature measured in the pixel where it peaks (see Sect. 3.2.1).

4.2. The Mrk 273 molecular outflow

As commented in Sect. 3.2.1, all the water lines observed with *Herschel*/PACS are consistently blue-shifted with respect to the systemic velocity of Mrk 273. The absorption is the various lines peaks in the range $[-20, -140]$ km s^{-1} and extends as far as -600 km s^{-1}. Velocity shifts are also observed in OH 65 μm and OH 84 μm (González-Alfonso et al. 2017), and trace the low-velocity gas of the approaching component of the outflow (González-Alfonso et al. 2017).

The channel maps of HCN and HCO$^+$ (Figs. 11 to 14) show clear emission elongated to the north and south. This seems to correspond to the red-shifted low velocity component (|v-v$_{sys}$|<400 km s^{-1}) of the wind heading to the north observed with CO (Cicone et al. 2014). In addition, we also see emission in the north-south direction at higher velocities (up to ∼400 km s^{-1}). In our data, we distinguish two velocity components of the outflow: one with relatively low velocities (|v-v$_{sys}$|<400 km s^{-1}) that is seen only in the channel maps (because its emission is blended with that of the disk in the spectra); and a high-velocity component (|v-v$_{sys}$|>400 km s^{-1}) that is seen in the spectrum of the central channel as a blue-shifted shoulder of the HCN (3 − 2) line (Fig. 5). The HCN (3 − 2) spectral bump spans approximately from -400 km s^{-1} to -1000 km s^{-1} (when centering the line at the rest frequency of HCN(3 − 2)), which is consistent with the outflow velocities measured with CO (Cicone et al. 2014).

As explained in Sect. 3.3.2, the size of the fast wind traced by HCN(3 − 2) is 0.″61 ± 0.″05 (∼460 pc) and the elongated shape towards the north can be seen clearly (Fig. 7). The CO (1 − 0) outflowing gas extends up to 550-600 pc in Mrk 273 (Cicone et al. 2014). This difference suggests that the expelled moderate density gas ($n_{H_2} \leq 10^3$cm^{-3}) travels further than the dense gas ($n_{H_2} \geq 10^4$cm^{-3}). In the right panel of Fig. 16 we show a sketch of the dense and warm outflow properties derived from our ob-

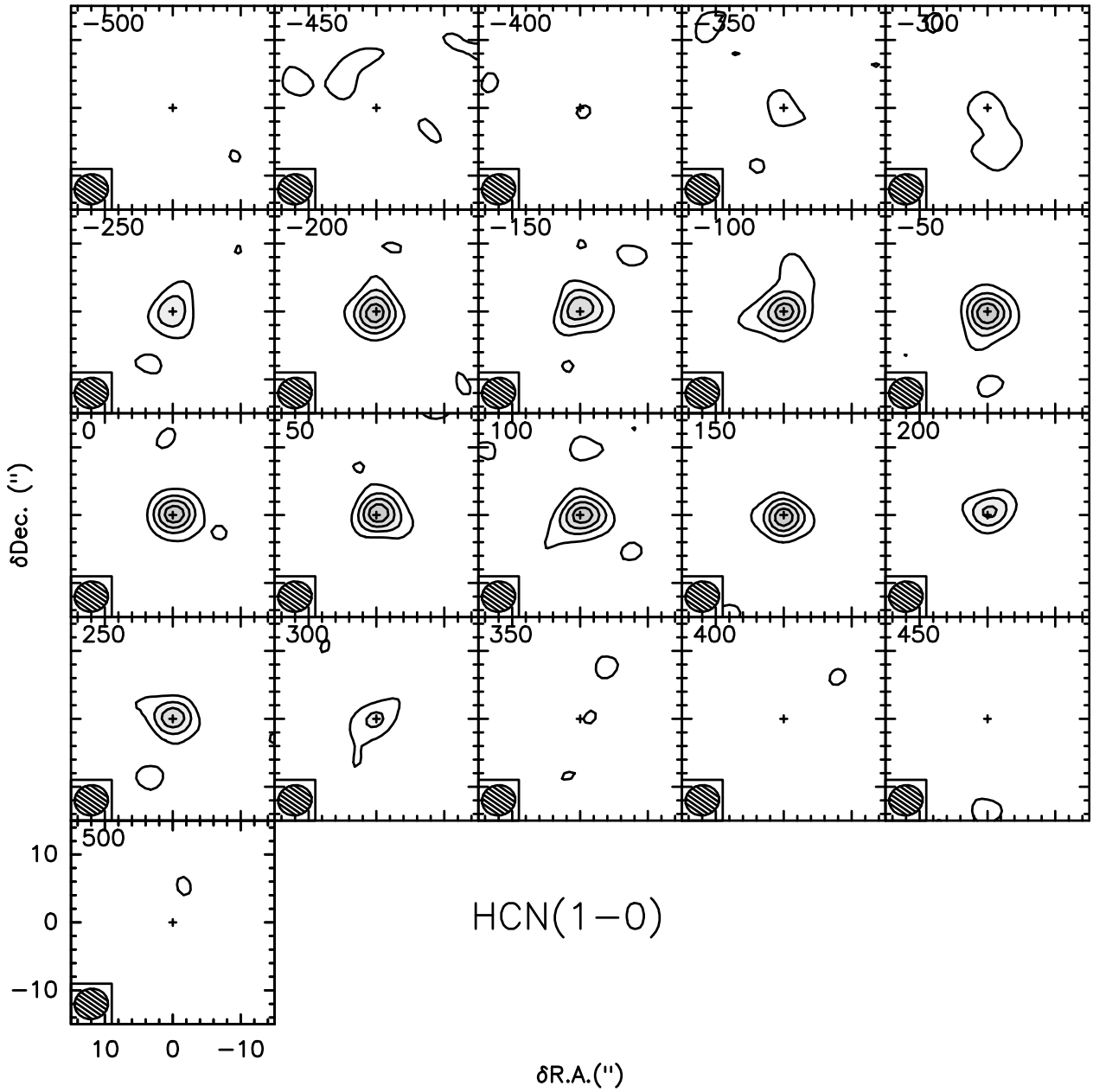

Fig. 11: Channel-velocity maps of HCN (1 − 0) in the velocity range [-500, 500] km s^{-1} with steps of 50 km s^{-1} . Contours go from 1.5 mJy beam^{-1} (5σ) to 9.5 mJy beam^{-1} with a spacing of 2 mJy beam^{-1}. The synthesised beam is plotted in the bottom left corner. North is up and east is to the left.

servations of Mrk 273, as well as the comparison with the diffuse phase of the outflow detected in CO by Cicone et al. (2014).

The HCN fast outflow luminosity is $L^{\rm outflow}_{\rm HCN(3-2)} = \pi R^2 I = 8\times10^7$ K km s^{-1} pc^2. To estimate the dense gas mass contained in the outflow we used the relation $M_{\rm dense} = 10 \times L'[HCN(3-2)]$ (Gao & Solomon 2004). We note that this formula might overestimate the actual value, because it assumes that all gas is virialised, which might not be the case in the outflow. Additionally, the HCN-to-H_2 conversion factor, which is not well constrained in ULIRGs, could also lead to an overestimation of the gas mass. A detailed analysis of the factors affecting the gas mass estimation can be found in Gao & Solomon (2004). We obtain $M^{\rm outflow}_{\rm dense} \leq 8\times10^8 M_\odot$, which is consistent with the value obtained from OH observations ($\sim1.6\times10^8 M_\odot$, González-Alfonso et al. 2017), and is also similar to the dense gas mass in the outflow of Mrk 231 ($\sim4\times10^8 M_\odot$, Aalto et al. 2015a). We note that our result refers only to the high-velocity gas (|v-$v_{\rm sys}$|>400 km s^{-1}), as it is not possible to separate the slow component of the outflow from the disk emission in the HCN data.

In cases where the outflow and the disk kinematics cannot be distinguished well in the velocity maps (as in our Fig. 8), a difference in their position angles can help to probe the kinematic decoupling between the two, and can also yield information about the nuclear powering source. Gas in starburst-powered outflows is always expelled perpendicular to the plane of the galaxy (thus showing a change of 90° respect to the P.A. of the starbursting disk), while AGN-powered outflows might virtually have any position angle, because the dusty torus and the accretion disk can be tilted with respect to the disk (García-Burillo et al. 2015). In Mrk 273, we measure a difference between the P.A. of the in-

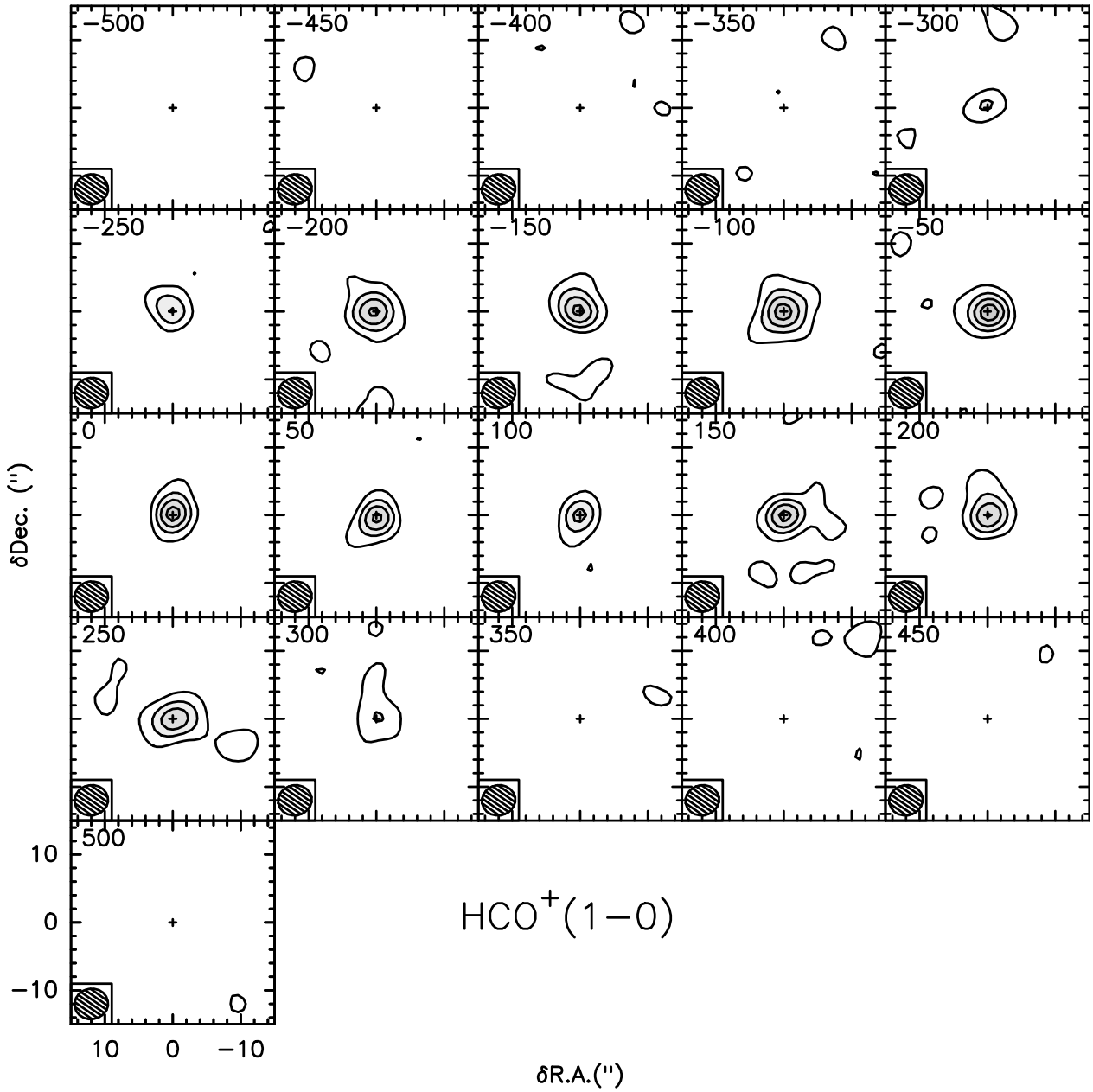

Fig. 12: Channel-velocity maps of $HCO^+(1-0)$ in the velocity range [-500, 500] km s^{-1} with steps of 50 km s^{-1} . Contours go from 1.5 mJy beam^{-1} (5σ) to 9.5 mJy beam^{-1} with a spacing of 2 mJy beam^{-1}. The synthesised beam is plotted in the bottom left corner. North is up and east is to the left.

ner disk (of 71° ± 5°, from $HCO^+(3-2)$, Table 3) and the P.A. of the outflow (10° ± 3°), of 60°±8°. This seems to indicate that the outflow is powered by the central AGN. Indeed, Cicone et al. (2014) found that the high outflow mass-loss rate of Mrk 273 is consistent with the linear correlation they observed between the bolometric AGN luminosity and the mass outflow rate in local AGN-host galaxies.

A couple of interesting issues arising from our data are 1) the red-shifted component of the outflow traced by HCN (3 − 2) is seen only at low velocities in the channel maps ($|v\text{-}v_{sys}|<$ 400 km s^{-1}). Indeed, a fast red-shifted wind, which should be visible in the spectra (with a similar intensity as the blue-shifted one), does not appear; and 2) the apparent absence of high-velocity winds in HCO^+ (i.e. HCO^+ line wings at $|v\text{-}v_{sys}|>$ 400 km s^{-1}). Regarding the first issue, deeper observations are required to improve the SNR of the outflow, to make sure that the red-shifted component is not present. If that would be the case, then it would imply that either there is a density or temperature gradient between the receding and the approaching gas (with the red-shifted gas being less dense and/or warm in general), or there is a chemical differentiation between the two. These are not uncommon characteristics in galactic winds, such as in Mrk 231 (Aalto et al. 2012, 2015a). The chemical differentiation could also explain why there is not enough high-velocity gas traced by HCO^+ in the outflow (see Lindberg et al. (2016) for details about this phenomena in the wind of Mrk 231).

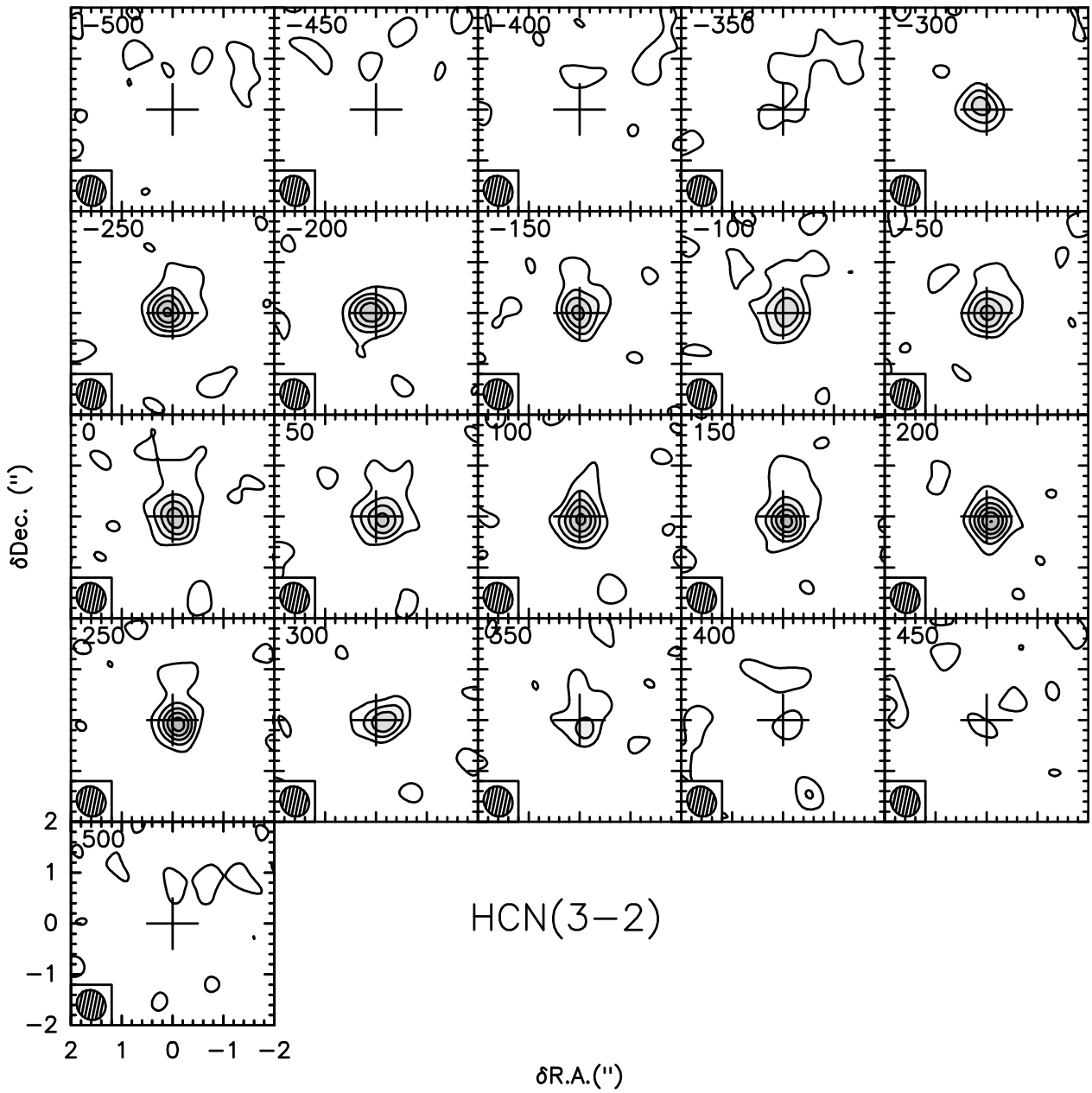

Fig. 13: Channel-velocity maps of HCN (3 − 2) in the velocity range [-500, 500] km s^{-1} with steps of 50 km s^{-1}. Contours go from 6.5 mJy beam^{-1} (5σ) to 56 mJy beam^{-1} with a spacing of 10 mJy beam^{-1}. Note the significant smaller spatial scale relative to the channel map of the (1 − 0) line shown in Fig. 11. The synthesised beam is plotted in the bottom left corner. North is up and east is to the left.

4.3. Expansion of the core

In Mrk 273, the velocity peaks of the OH 65 μm and OI 63 μm lines are shifted in comparison to the emission peak of [CII] at 158 μm (González-Alfonso et al. 2017). The [CII] maximum is found at zero velocities (with respect to the systemic velocity of the galaxy), and arises from the bulk of the warm gas in the nucleus. The OH 65 μm and OI 63 μm lines, however, have their maximum (absorption/emission) peaks shifted by ±50 km/s, and trace the blue component of the outflowing gas moving at low velocities. Apart from being a sign of a superwind, González-Alfonso et al. (2017) argue that this change in the redshift also indicates that the large columnns of gas close to the central engine are expanding at low velocities. This effect has been found in a number of other ULIRGs where low velocity outflows are also present (González-Alfonso et al. 2017).

As discussed in Sect. 4.1, the shift of approximately 50 km s^{-1} seen in OH 65 μm and OI 63 μm also appears in our H_2O data. In particular, the H_2O lines observed with PACS, which according to our models trace the compact core with a radius ∼50 pc, are also blue-shifted with respect to [CII] by [−20, −140] km s^{-1} (Table 2). This indicates that, apart from rotating, the gas in the core is expanding at low velocities, pushing outwards the boundaries with the inner disk traced by the HCN and HCO^+(3 − 2) lines. Indeed, the expansion is also reflected in our HCO^+ and HCN(3 − 2) data. While HCO^+ and HCN(3 − 2) double-peaks probe the outer edges of the inner disk (at a radius ∼300 pc), their peaks of absorption probe the kinematics of

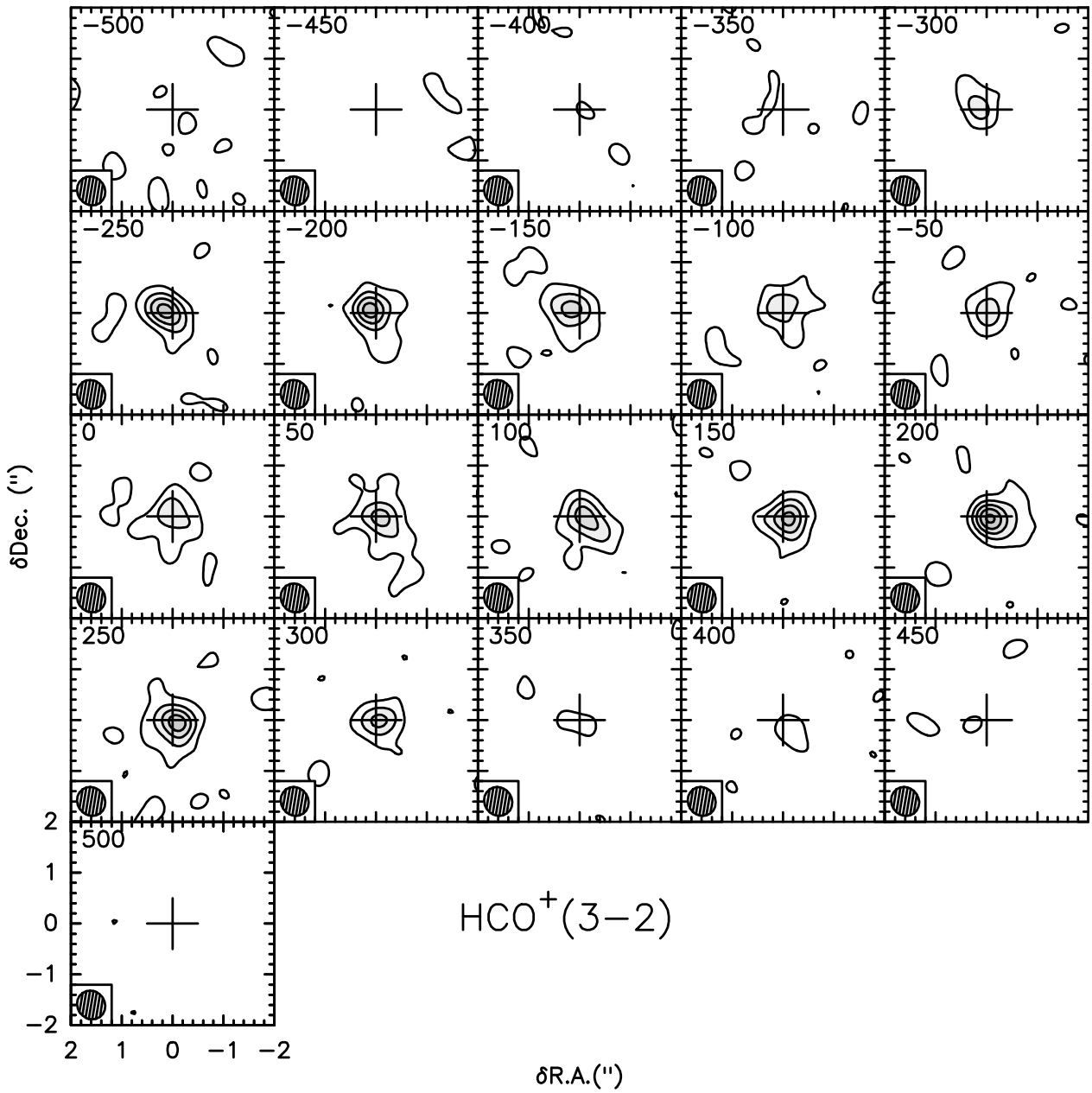

Fig. 14: Channel-velocity maps of $HCO^+(3-2)$ in the velocity range [-500, 500] km s^{-1} with steps of 50 km s^{-1}. Contours go from 6.5 mJy beam^{-1} (5σ) to 56 mJy beam^{-1} with a spacing of 10 mJy beam^{-1}. Note the significant smaller spatial scale relative to the channel maps of the (1 − 0) line shown in Fig. 12. The synthesised beam is plotted in the bottom left corner. North is up and east is to the left.

the bulk of the disk, which is also shifted by 50-100 km s^{-1}. We interpret this as the gas in the inner disk being pushed by the expanding gas of the core. We illustrate this in the sketch shown in the right panel of Figure 16.

4.4. Non-detection of vibrational emission

Rotational transitions within vibrationally excited levels of HCN and HC_3N have been observed in the central <100 pc of several (U)LIRGs, probing regions of high temperatures of ≥100 K (Sakamoto et al. 2010; Costagliola et al. 2015; Aalto et al. 2015b; Martín et al. 2011, 2016), and high column densities. Their excitation cannot be explained by collisional effects alone, and mid-infrared pumping is necessary in order to populate the upper energy levels and fit their observed luminosities (Aalto et al. 2015b). In that case, the vibrational lines may be more suitable to study the optically thick dust cores of galaxies than the rotational transitions (see Aalto et al. (2015b) for a detailed discussion).

In our NOEMA observations of Mrk 273, we do not detect the vibrationally excited line HCN(3 − 2) v_2=1. The line is split into two components with energy levels of similar intensity, v2=1e and v2=1f, at frequencies 265.8 and 267.2 GHz. The first one is completely blended with the HCN (3 − 2) rotational line due to the galactic broad linewidths, and it is not possible to estimate its peak temperature. However, the v_2=1f transition would appear as a bump only partially blended with the red side of the $HCO^+(3-2)$ transition. We calcu-

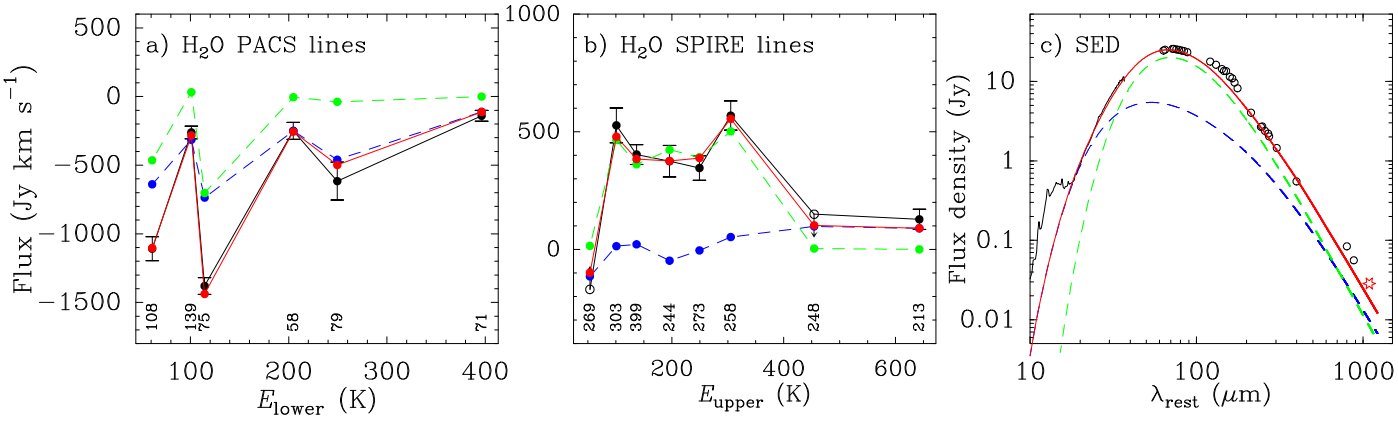

Fig. 15: Comparison between the observed (black symbols) and modelled (coloured symbols and lines) H_2O fluxes in Mrk 273 within a) PACS and b) SPIRE. The model includes 2 components; the core (in blue), which accounts for most absorption lines observed within PACS, and the inner disk (in green), which dominates the emission of the sub-mm lines with $E_{\rm upper} < 400$ K observed with SPIRE (see Table 4). Red colours and symbols indicate total modelled fluxes. The numbers at the bottom of panels a and b indicate rounded-up transition wavelengths in μm. c) The spectral energy distribution (SED) of Mrk 273, including the *Spitzer*/IRS spectrum, *Herschel*/PACS and SPIRE continuum data from observations of both H_2O and OH lines, sub-mm data at 800 and 880 μm (Rigopoulou et al. 1996; Wilson et al. 2008), and our measured flux density at 1mm (starred-red symbol), is compared with the prediction of our composite model.

Table 6: Nuclear brightness temperature ratios in Mrk 273 (row/column), evaluated in the central pixel.

	HCN(1 − 0)	HCO^+(1 − 0)	HNC(1 − 0)	HC_3N(10 − 9)	HCN(3 − 2)	HCO^+(3 − 2)	HOC^+(3 − 2)†
HCN(1 − 0)	1.00±0.07	1.03±0.07	2.2±0.2	9±2	—	—	—
HCO^+(1 − 0)	0.97±0.06	1.00±0.07	2.1±0.2	9±2	—	—	—
HNC(1 − 0)	0.45±0.04	0.46±0.04	1.0±0.1	4±1	—	—	—
HC_3N(10 − 9)	0.11±0.02	0.12±0.03	0.25±0.06	1.0±0.3	—	—	—
HCN(3 − 2)	—	—	—	—	1.00±0.06	1.28±0.08	7±3
HCO^+(3 − 2)	—	—	—	—	0.78±0.05	1.00±0.07	5±3
HOC^+(3 − 2)†	—	—	—	—	0.14±0.07	0.18±0.09	1.0±0.7

Notes: Due to differences in the observed areas, we do not list the ratios between the 3 mm and 1 mm lines (see Sect. 4.5). † For HOC^+(3 − 2) we used the temperature measured in the pixel where it peaks (see Sect. 3.2.1).

Table 7: Main parameters of the undetected vibrational transitions of HCN and HC_3N.

Line	Freq [GHz]	$E_{\rm low}$ [K]	A_{ul} [$\times10^{-3}$s^{-1}]	$n_{\rm crit}$ [cm^{-3}]	Flux [K km s^{-1}]	Line Peak [mJy]	L′ [K km s^{-1} pc^2]
HC_3N (10 − 9) v_6=1	91.202	512	0.15	$> 10^{11}$	≤1.1	≤0.3	≤6.4×10^6
HCN (3 − 2) v_2=1	267.199	720	0.73	$> 10^{10}$	≤3.7	≤1.1	≤7.3×10^5

late a limit to its flux density in the central pixel of 1.1 mJy, which is slightly below the 1σ rms level (of 1.2 mJy, calculated at the final velocity resolution). Assuming that the vibrational line has the same FWHM as the HCN rotational transition (~600 km s^{-1}), the limit to the integrated intensity was estimated as $I \leq 3 \times rms \times \sqrt{FWHM \times Dv}$ =4 K km s^{-1} (Dv, the final spectral resolution, is 68 Km s^{-1}). Under the conservative assumption that both rotational and vibrational lines have the same source size, the upper limit to the HCN-vib luminosity is $L' = \pi R^2 I \leq 7.3 \times 10^5$ K km s^{-1}pc^2 (R is the source size of the HCN (3 − 2) emission specified in Table 3). This is at least a factor of two fainter than the $L'_{\rm HCN_{vib}(3-2)}$ in Mrk 231 (1.7×10^7 K km s^{-1}pc^2, Aalto et al. 2015a). This is interesting, because Lahuis et al. (2007) detect the 14μm HCN-vib lines in absorption at the same level in both Mrk 273 and Mrk 231.

Aalto et al. (2015b) found a tentative correlation between the outflow velocity and the intensity of HCN vibrationally excited lines in a moderate sample of ten (U)LIRGs. Galaxies with fast outflows (i.e. when the outflow velocity exceeds the escape velocity of the nuclear region) tend to have fainter vibrational lines. With its non detection of HCN(3 − 2) v_2=1, and its fast molecular outflow, Mrk 273 also follows this relationship. The reason for this correlation, if true, needs further investigation.

Similarly, we do not detect the vibrationally excited line HC_3N (10 − 9) v_6=1, even though the energy of its lower level is below that of the HCN-vib lines (Table 7). We obtain an upper limit to the peak flux density of 0.3 mJy. This line was first tentatively detected in the LIRG NGC 4418 with the IRAM 30 m telescope (Aalto et al. 2007; Costagliola & Aalto 2010) and later confirmed by ALMA observations (Costagliola et al. 2015) with a rotational-to-vibrational intensity ratio of ~11 . If we extrapolate that ratio to Mrk 273 then, based on our results, one would expect a flux density of ~0.2 mJy. Under the assumption that in Mrk 273 HC_3N(10 − 9) v_6=1 likely arises from a region smaller

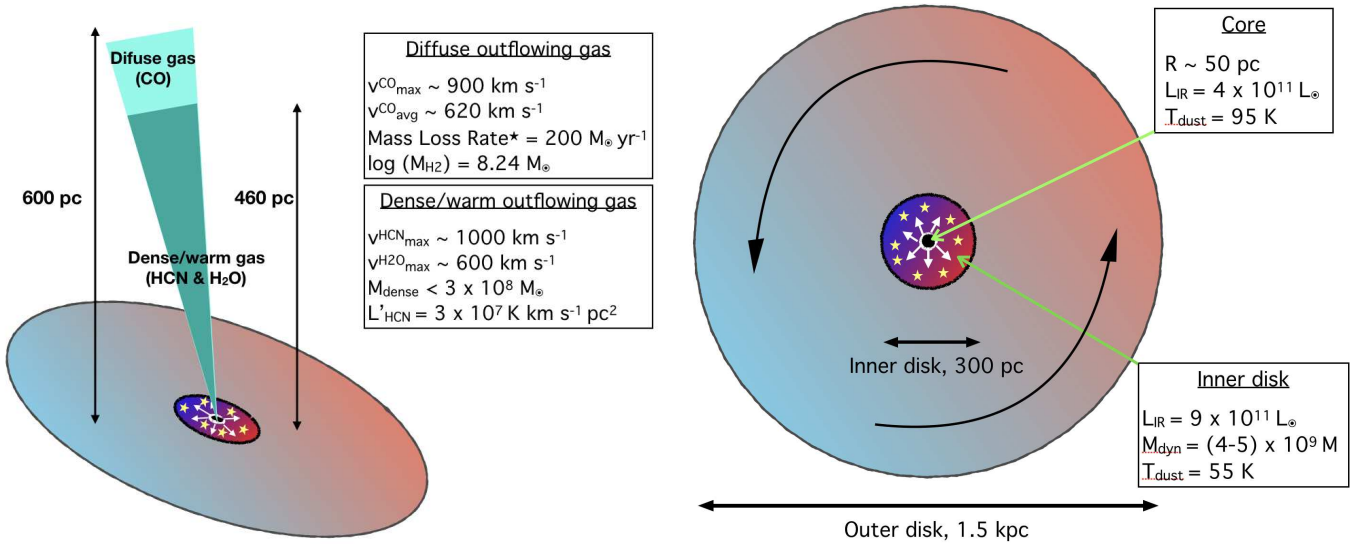

Fig. 16: Left: Sketch of the blue-shifted molecular outflow in the northern nucleus of Mrk 273. The dense and warm outflowing gas found in our HCN and H_2O data, and its properties, is compared to the diffuse outflow found by Cicone et al. (2014) by observing CO (1 − 0). ⋆Note that the mass loss rate is calculated as $\dot{M}=v\,(M_{OF}/R_{OF})$ (see Sect. 5.5 in González-Alfonso et al. 2017), which is a factor 3 lower than the value given by Cicone et al. (2014). The position angles of the outflow (10°) and the inner disk (70°) are represented. Right: A face-on sketch of the three disk components identified in our data (outer disk, inner disk, and core), which are plotted in scaled sizes. The decoupled kinematics of the outer and inner disks are represented by the blue and red colours, which depict the orientation of the blue-shifted and red-shifted rotating gas. The rotation direction is indicated by the curved arrows. The intensity of the colours illustrate the velocities, hence the inner disk rotates at higher speed than the outer disk. The stars in the inner disk aim to show the region where most of the starburst is located. The radial arrows represent the low-velocity expansion of the core.

than HCN(1 − 0) (i.e. $\theta < 2''.0 \times 1''.6$), the limit to its luminosity is 6×10^6 K km s^{-1} pc^2.

Apart from sensitivity issues, two possibilities can potentially explain why we do not detect vibrationally excited emission of HCN and HC_3N in Mrk 273. One is that the mid-infrared radiation density in the core of Mrk 273 is not as strong as in other galaxies hosting compact obscured nuclei, such as Mrk 231, Arp 220 or NGC 4418. The other is that, although the mid-IR radiation is strong, the obscuration in the centre of Mrk 273 is so high that even the emission of vibrationally excited lines is extincted.

4.5. Molecular line ratios

Tables 5 and 6 list the brightness temperature ratios of the species detected with NOEMA. The ratios were obtained by comparing the temperatures of the lines calculated over the entire emission (Table 5) and in the central pixel (Table 6). Note that the 3 mm lines (HCN, HCO^+, HNC(1-0) and HC_3N(10-9)) and the 1 mm lines (HCN, HCO^+, HOC+(3 − 2)) were observed with angular resolutions that differ in the covering area by a factor >60 of covering area. In order to avoid confusion and unphysical results, we only discuss ratios in which both lines were observed with the same resolution. In the following we discuss the most relevant ratios.

4.5.1. HCN/HCO^+

The integrated intensity ratio between HCN and HCO^+ has been widely used to discriminate between starburst-powered galaxies and AGNs (Kohno et al. 2001; Krips et al. 2008; Imanishi et al. 2009; Izumi et al. 2013, 2016; Martín et al. 2015). An enhancement of the HCN abundance with respect to HCO^+ is observed in a fairly large sample of Seyferts, which show a HCN/HCO^+ ratio ≥ 1. Starbursts, on the other hand, are found to have values ≤ 1. The coexistence of both phenomena in the central few hundred parsec can however lead to outlier values of the ratio if they are not resolved (Aladro et al. 2015; Privon et al. 2015).

The reason why the HCN/HCO^+ ratio is a diagnostic of the galactic central activity is still debated. For more than a decade, the HCN enhancement was claimed to be due to X-ray irradiation in the vicinity of the SMBHs (e.g. Kohno et al. 2001). However, recent studies of NGC 1097 point to high temperatures and/or mechanical heating as a more plausible explanation (Martín et al. 2015; Izumi et al. 2016). Systematic high-angular resolution observations of a larger sample of galaxies/AGNs is still needed to clarify this issue.

In the case of HCO^+, both observations and models point to an enhancement in starburst galaxies, and in particular in photon-dominated regions (PDRs), as a result of strong UV irradiation. Unfortunately, the scenario could be more complex, since chemical models suggest that HCO^+ can also be enhanced in regions heavily pervaded by cosmic ray/X-ray fields, such as in AGNs (Meijerink et al 2006, Aladro et al. 2013). Yet this scenario has not been confirmed with observations, to our knowledge.

Bearing in mind that the reasons for the enhancements of HCN and HCO^+ are difficult to assess, the fact is that this ratio diagnoses the power sources of many well-known active galaxies. Nevertheless, there are some sources which do not seem to be consistent with this scenario. For example, some apparent starbursts have HCN-to-HCO^+ ratios as high as AGNs, indicating that the HCN enhancement cannot be exclusively attributed to AGNs (Privon et al. 2015).

In Mrk 273, we measure the global brightness intensity ratios HCN(1 − 0)/HCO^+(1 − 0)= 1.0±0.2 and HCN(3 − 2)/HCO^+(3 −

2)= 1.1±0.3 (Table 5). Evaluating the nuclear ratios in the central pixel, gives very similar values of 1.0±0.2 and 1.3±0.3 for the (1 − 0) and (3 − 2) transitions respectively (Table 6). These ratios place the galaxy in an ambiguous region of the diagnostic diagram, where a starburst, an AGN, or a combination of the two are possible. Depending on the diagnostic used in the literature, either an AGN or a starburst are claimed to power the northern nucleus of Mrk 273. Perhaps a mixture of both activities are present in the central hundred parsecs. Unfortunately, our HCN/HCO^+ ratio does not help to elucidate the nature of the Mrk 273 nuclear source. Nevertheless, we note that both lines are significantly affected by opacity (Sect. 4.1), and that a more thorough analysis of this ratio including obscuration effects could further elucidate our results.

Using the Nobeyama Millimeter Array and RAINBOW interferometers at the Nobeyama Radio Observatory [6], Imanishi et al. (2006) obtained a flux ratio HCN(1 − 0)/HCO^+(1 − 0) >1.8 in Mrk 273, within a beam of 1.″9×1.″5. This was interpreted as a signature of an AGN-dominated nucleus. This lower limit is much higher than our values, but we note that they did not detect HCO^+(1 − 0), and that their HCN(1 − 0) and continuum fluxes are 70-80% lower than our values.

4.5.2. HCN/HNC and HCO^+/HNC

Some (U)LIRGs, such as Arp 220 and Mrk 231, are extremely bright in HNC, with line intensities almost equal or even surpassing those of HCN (Huettemeister et al. 1995; Aalto et al. 2002; Aladro et al. 2015). Several scenarios can produce this unusually high line ratio, such as chemical reactions at moderate densities and temperatures (n∼10^4 – 10^5cm^{-3}, T_{kin} ∼50 K), high opacities of HCN with respect to HNC and, very likely, infrared pumping affecting HNC more than HCN (Aalto et al. 2002). The HCN/HNC intensity ratio can reflect the evolutionary stage of starburst regions in galactic centres, with faint HNC emission (i.e. HCN/HNC ≫ 1) being associated with shock-dominated regions, which are common in early starbursts (Aladro et al. 2015).

The brightness temperature ratio between HCN(1 − 0) and HNC(1 − 0) in Mrk 273 is 1.7 (2.1 in the central pixel). Previous observations of these lines with the OSO and SEST single-dish telescopes yielded an integrated intensity ratio ≥4 (Aalto et al. 2002), although that value is based on an upper limit to the HNC line. Taking our result of 1.7 as the minimum value, it is safe to say that this conservative ratio is moderately high, and that Mrk 273 cannot be classified as an HNC-luminous galaxy.

As discussed above (Sect. 4.5.1), the HCN/HCO^+ brightness temperature ratio we obtain for Mrk 273 does not allow us to favour a starburst over an AGN-dominated nucleus. The HNC and HCO^+ intensities appear to be anti-correlated in (U)LIRGs, as observed by Costagliola et al. (2011) in a fairly large sample of galaxies. From our data, we obtain an HCO^+/HNC = 1.8 ± 0.2 (Table 6). If the northern nucleus of Mrk 273 is dominated by a starburst (as claimed by Condon et al. 1991; Majewski et al. 1993; Downes & Solomon 1998), the low HNC abundance would indicate that the gas comes from warm and dense phases in an early stage, and would explain why HCO^+ is relatively abundant. However, models by Rodríguez Zaurín et al. (2009) indicate that most of the stellar population in Mrk 273 has an age of 0.7-10 Gyr (although there might be a significant fraction of stars younger than 50 Myr), which challenges an early starburst scenario. In the case of an AGN (as claimed by U et al. 2013; Rodríguez Zaurín et al. 2014; Iwasawa et al. 2017), HNC does not necessarily need to be faint, but HCN could be boosted. However, in the latter scenario one would expect a higher HCN/HCO^+ ratio.

[6] https://www.nro.nao.ac.jp/en/astronomer/

4.5.3. An extremely low HCO^+/HOC^+ ratio

HOC^+, the metastable isomer of HCO^+, is efficiently formed via the following ion-molecule reactions

$$CO^+ + H_2 \rightarrow HOC^+ + H, \quad (4)$$

$$C^+ + H_2O \rightarrow HOC^+ + H, \quad (5)$$

$$H_3^+ + CO \rightarrow HOC^+ + H_2, \quad (6)$$

and is mainly destroyed by reactions with H_2 (Jarrold et al. 1986; Smith et al. 2002; Fuente et al. 2003):

$$HOC^+ + H_2 \rightarrow HCO^+ + H_2. \quad (7)$$

While typical values of the HCO^+/HOC^+ ratio in Galactic dense molecular clouds range between 300 and 6000 (Apponi et al. 1997), values as low as 50-150 are found in several Galactic and extragalactic PDRs and XDRs (X-ray dominated regions), likely as a consequence of high ionisation rates created by ionisation fields (UV, cosmic rays, and/or X-ray radiation). Fuente et al. 2003; Usero et al. 2004). From our observations, we derive a global brightness temperature ratio $HCO^+(3-2)/HOC^+(3-2)$ = 9 ± 4, and a nuclear ratio of 5 ± 3. Such low values have only been found in other ULIRGs hosting extremely compact obscured nuclei, namely IC 860, Zw049.057 and Mrk 231 (Aalto et al. 2015a,b). The physical and chemical reasons for these low ratios are still not known and deserve further study, but high opacities of HCO^+ could be responsible.

4.6. A different origin of HOC^+ emission

As mentioned in Sect. 3.3, HOC^+(3 − 2) peaks at RA (J2000) = 13^h:44^m:$42^s.15$, DEC (J2000) = 55°:53′:13.″45, which corresponds to an offset (0.″2, −0.″05) south-east of the central pixel. This indicates that its emission has a different origin than the rest of the dense gas tracers. Furthermore, the two HOC^+ components are blue-shifted in velocity with respect to HCN and HCO^+(3 − 2) (Table 1). Fig. 17 shows the HOC^+ emission in contours plotted over the blue-shifted HCO^+ emission integrated between -300 and 0 km s^{-1}. This plot shows that HOC^+ does not peak at the same position as the blue-shifted dense gas, and that there is not even detected emission of the species in the central pixel.

Why is the emission of this species shifted with respect to the others? One possibility is that the central pixels are heavily obscured and HOC^+ is completely absorbed there. However, in that case one would expect some kind of symmetric emission around the nucleus, with a ring-like shape, or at least other peaks of emission around the nucleus, which are not seen. This strongly suggests that HOC^+ is not peaking at the very centre.

We checked the literature looking for OH masers, supernovae, radio continuum sources, or any source emitting at the HOC^+ peak coordinates. High-angular resolution near-IR observations conducted by U et al. (2013) resolve the northern nucleus

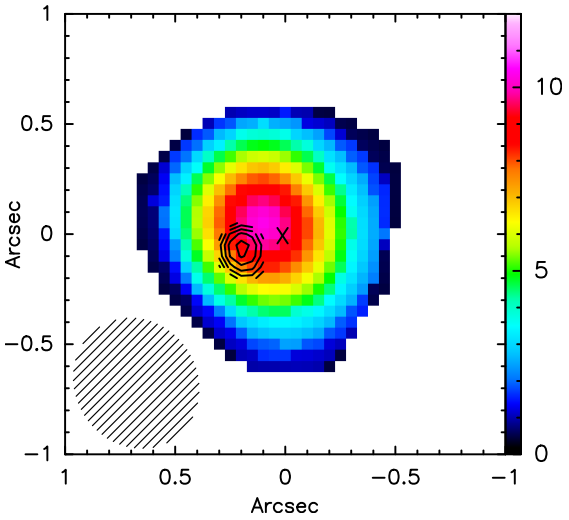

Fig. 17: $HCO^+(3-2)$ blue-shifted intensity colours (in units of Jy km s^{-1} beam^{-1}) integrated from -300 km s^{-1} to 0 km s^{-1} with $HOC^+(3-2)$ contours (starting from 3σ=3.3 mJy beam^{-1}) overplotted with steps of 10 mJy beam^{-1}. The cross at the centre marks the continuum peak. The synthesised beam is shown in the bottom left corner.

of Mrk 273 into three components, called N1, N2, and N3. N1 is the brightest of the three and is associated with the true nucleus (our (0″, 0″) position). N3 is found ∼0.″15 to the south-east of N1, very near the HOC^+ maximum flux density. The peak of the HOC^+ emission might correspond to N3, but better astrometry is needed in order to strengthen this association. The nature of N3 is, in any case, not clear, but it does have stronger emission from [FeII] than N1. It could be a separated clump, a compact star cluster, or a supernova remnant. N3 does not appear in radio continuum maps (Carilli & Taylor 2000; Bondi et al. 2005), leaving a supernova remnant as a less likely option. To further address the origin of this species, deeper high-resolution observations of HOC^+ would be needed to determine its extent and to more accurately measure its position.

5. Conclusions

We have used the NOEMA interferometer to observe several spectral lines of HCN, HCO^+, HOC^+, HNC, and HC_3N with angular resolutions of (4.″9×4.″5) and (0.″61×0.″55) (corresponding to spatial scales of ∼(3.7×3.4) kpc and ∼(460×420) pc). We also included multiple lines of H_2O observed with the *Herschel* SPIRE and PACS instruments. Our observations, extending from the mm to the far-IR regime, allowed us to study the properties of the gaseous disk in the northern nucleus of Mrk 273, as well as the connection between its cold and warm phases. We summarise the main results as follows:

– **Morphology and kinematics of the disk.** The cold and dense gas in the nuclear disk (traced by HCN and HCO^+) has two components with decoupled kinematics. The low excitation gas in the outer parts of the disk, extends up to a radius of ∼1.5 kpc and rotates from south-east to north-west (with a P.A. of approximately −40°), while the more excited dense gas arising from the central star-forming region (<300 pc) is characterised by a north-east to south-west rotation (P.A.∼70°). This inner disk contains a dynamical mass of $3\times10^9 M_\odot$, and a luminosity of $L'_{\rm HCN}$ = 3×10^8 K km s^{-2} pc^2. The warm gas, traced by the far-IR H_2O lines, can also be separated into two components: a warm and very compact core with a radius ∼50 pc and a temperature of 95 K, and a more extended and relatively cooler component, with R <300 pc and T = 55 K.
The extended component of the warm gas and the compact component of the cold gas are co-spatial in the inner ∼300 pc. The H_2 column densities and dust properties obtained from our water modelling, as well as the line profiles of the dense gas tracers, show that this region is significantly affected by dust obscuration. The blue-shifted emission of the bulk of gas (consistently seen in all observed lines) also indicates that the core is expanding outwards at low velocities (v-v_{sys} ∼ 50-100 km s^{-1}), likely affected by the outflow.
– **Outflow properties.** We detected the cold (sub-mm) and warm (far-IR) phases of the Mrk 273 molecular outflow. It is a compact outflow, being expelled to distances ∼460 pc mostly towards the northern direction, but it reaches high velocities of ∼1000 km s^{-1}. This fast outflow (|v-v_{sys}|>400 km s^{-1}) has a luminosity of 8×10^7 K km s^{-1} pc^2, and a mass of dense gas $M^{\rm outflow}_{\rm dense}$ ≤$8\times10^8 M_\odot$. The difference in P.A. between the major kinematic axis of the inner disk (71° ± 5°) and that of the outflow (10° ± 3°) suggests that the latter is probably driven by the AGN.
– **Chemistry.** We explored the chemistry of Mrk 273 by means of molecular line ratios. The most outstanding ratio is that of HCO^+/HOC^+. We estimated it to be <10, therefore being one of the lowest values ever measured in any galactic or extragalactic source. The reason, however, is still not clear and should be further studied in detail with the help of chemical models. Yet it is worth noting that the origin of HOC^+ is different from the rest of the detected molecular species, since its emission is spatially shifted from the centre.
Regarding the outflow, our non detection of the high-velocity wind in HCO^+, together with the non-detection of the redshifted outflowing gas either in HCN and HCO^+, suggests the possibility of chemical differentiation. However, we note that, despite our high sensitivity, the fast outflow of Mrk 273 is very faint, so deeper observations would be necessary to better probe its chemistry.

Acknowledgements. This work is based on observations carried out under project numbers W14DD and E16AK with the IRAM NOEMA Interferometer. IRAM is supported by INSU/CNRS (France), MPG (Germany) and IGN (Spain). The research leading to these results has received funding from the European Union's Horizon 2020 research and innovation program under grant agreement No 730562 [RadioNet]. This research has made use of NASA's Astrophysics Data System, and the NASA/IPAC Extragalactic Database (NED), which is operated by the Jet Propulsion Laboratory, California Institute of Technology, under contract with the National Aeronautics and Space Administration. We are grateful to the referee for the fast and constructive report, as well as to the IRAM/NOEMA staff for their help during the observations and data reduction. RA would like to thank Leslie Hunt and Loreto Barcos-Muñoz for the useful discussions about Mrk 273.

References

Aalto, S., Polatidis, A. G., Hüttemeister, S., & Curran, S. J. 2002, A&A, 381, 783
Aalto, S., Monje, R., & Martín, S. 2007, A&A, 475, 479
Aalto, S., Garcia-Burillo, S., Muller, S., et al. 2012, A&A, 537, A44
Aalto, S., Garcia-Burillo, S., Muller, S., et al. 2015a, A&A, 574, A85
Aalto, S., Martín, S., Costagliola, F., et al. 2015b, A&A, 584, A42
Aalto, S., Muller, S., Costagliola, F., et al. 2017, A&A, 608, A22
Aladro, R., Martín-Pintado, J., Martín, S., Mauersberger, R., & Bayet, E. 2011, A&A, 525, A89
Aladro, R., Viti, S., Bayet, E., et al. 2013, A&A, 549, A39

Aladro, R., Martín, S., Riquelme, D., et al. 2015, A&A, 579, A101
Apponi, A. J., & Ziurys, L. M. 1997, ApJ, 481, 800
Armus, L., Charmandaris, V., Bernard-Salas, J., et al. 2007, ApJ, 656, 148
Bondi, M., Pérez-Torres, M.-A., Dallacasa, D., & Muxlow, T. W. B. 2005, MNRAS, 361, 748
Botinelli, L., Fraix-Burnet, D., Gouguenheim, L., Le Squeren, A. M., & Patey, I. 1985, IAU Circ., 4074, 1
Carilli, C. L., & Taylor, G. B. 2000, ApJ, 532, L95
Cicone, C., Maiolino, R., Sturm, E., et al. 2014, A&A, 562, A21
Cole, G. H. J., Pedlar, A., Holloway, A. J., & Mundell, C. G. 1999, MNRAS, 310, 1033
Colina, L., Arribas, S., & Borne, K. D. 1999, ApJ, 527, L13
Condon, J. J., Huang, Z.-P., Yin, Q. F., & Thuan, T. X. 1991, ApJ, 378, 65
Condon, J. J. 1997, PASP, 109, 166
Costagliola, F., & Aalto, S. 2010, A&A, 515, A71
Costagliola, F., Aalto, S., Rodriguez, M. I., et al. 2011, A&A, 528, A30
Costagliola, F., Sakamoto, K., Muller, S., et al. 2015, A&A, 582, A91
Daniel, F., Dubernet, M.-L., & Grosjean, A. 2011, A&A, 536, A76
Davies, R. I., Tacconi, L. J., & Genzel, R. 2004, ApJ, 613, 781
Downes, D., & Solomon, P. M. 1998, ApJ, 507, 615
Dubernet, M.-L., Daniel, F., Grosjean, A., & Lin, C. Y. 2009, A&A, 497, 911
Falstad, N., González-Alfonso, E., Aalto, S., & Fischer, J. 2017, A&A, 597, A105
Fuente, A., Rodrıguez-Franco, A., Garcıa-Burillo, S., Martın-Pintado, J., & Black, J. H. 2003, A&A, 406, 899
Gao, Y., Gruendl, R. A., Hwang, C.-Y., & Lo, K. Y. 1999, Galaxy Interactions at Low and High Redshift, 186, 227
Gao, Y., & Solomon, P. M. 2004, ApJS, 152, 63
García-Burillo, S., Combes, F., Usero, A., et al. 2015, A&A, 580, A35
González-Alfonso, E., & Cernicharo, J. 1997, A&A, 322, 938
González-Alfonso, E., & Cernicharo, J. 1999, ApJ, 525, 845
González-Alfonso, E., Fischer, J., Isaak, K., et al. 2010, A&A, 518, L43
González-Alfonso, E., Fischer, J., Aalto, S., & Falstad, N. 2014, A&A, 567, A91
González-Alfonso, E., Fischer, J., Spoon, H. W. W., et al. 2017, ApJ, 836, 11
Griffin, M. J., Abergel, A., Abreu, A., et al. 2010, A&A, 518, L3
Huettemeister, S., Henkel, C., Mauersberger, R., et al. 1995, A&A, 295, 571
Imanishi, M., Nakanishi, K., & Kohno, K. 2006, AJ, 131, 2888
Imanishi, M., Nakanishi, K., Tamura, Y., & Peng, C.-H. 2009, AJ, 137, 3581
Imanishi, M., Nakanishi, K., & Izumi, T. 2016, AJ, 152, 218
Ivison, R. J., Greve, T. R., Dunlop, J. S., et al. 2007, MNRAS, 380, 199
Iwasawa, K., U, V., Mazzarella, J. M., et al. 2017, arXiv:1711.01750
Izumi, T., Kohno, K., Martín, S., et al. 2013, PASJ, 65, 100
Izumi, T., Kohno, K., Aalto, S., et al. 2016, ApJ, 818, 42
Janssen, A. W., Christopher, N., Sturm, E., et al. 2016, ApJ, 822, 43
Jarrold, M. F., Bowers, M. T., Defrees, D. J., McLean, A. D., & Herbst, E. 1986, ApJ, 303, 392
Kohno, K., Matsushita, S., Vila-Vilaró, B., et al. 2001, The Central Kiloparsec of Starbursts and AGN: The La Palma Connection, 249, 672
Krips, M., Neri, R., García-Burillo, S., et al. 2008, ApJ, 677, 262-275
Lahuis, F., Spoon, H. W. W., Tielens, A. G. G. M., et al. 2007, ApJ, 659, 296
Lindberg, J. E., Aalto, S., Muller, S., et al. 2016, A&A, 587, A15
Lu, N., Zhao, Y., Díaz-Santos, T., et al. 2017, ApJS, 230, 1
Majewski, S. R., Hereld, M., Koo, D. C., Illingworth, G. D., & Heckman, T. M. 1993, ApJ, 402, 125
Martín, S., Mauersberger, R., Martín-Pintado, J., Henkel, C., & García-Burillo, S. 2006, ApJS, 164, 450
Martín, S., Krips, M., Martín-Pintado, J., et al. 2011, A&A, 527, A36
Martín, S., Kohno, K., Izumi, T., et al. 2015, A&A, 573, A116
Martín, S., Aalto, S., Sakamoto, K., et al. 2016, A&A, 590, A25
Medling, A. M., U, V., Guedes, J., et al. 2014, ApJ, 784, 70
Meijerink, R., Spaans, M., & Israel, F. P. 2006, ApJ, 650, L103
Nardini, E., Risaliti, G., Salvati, M., et al. 2009, MNRAS, 399, 1373
Ott, S. 2010, Astronomical Data Analysis Software and Systems XIX, 434, 139
Pickett, H. M., Poynter, R. L., Cohen, E. A., et al. 1998, J. Quant. Spectr. Rad. Transf., 60, 883
Poglitsch, A., Waelkens, C., Geis, N., et al. 2010, A&A, 518, L2
Privon, G. C., Herrero-Illana, R., Evans, A. S., et al. 2015, ApJ, 814, 39
Rangwala, N., Maloney, P. R., Wilson, C. D., et al. 2015, ApJ, 806, 17
Rigopoulou, D., Lawrence, A., & Rowan-Robinson, M. 1996, MNRAS, 278, 1049
Rodríguez Zaurín, J., Tadhunter, C. N., & González Delgado, R. M. 2009, MNRAS, 400, 1139
Rodríguez Zaurín, J., Tadhunter, C. N., Rupke, D. S. N., et al. 2014, A&A, 571, A57
Sakamoto, K., Aalto, S., Evans, A. S., Wiedner, M. C., & Wilner, D. J. 2010, ApJ, 725, L228
Savage, C., & Ziurys, L. M. 2004, ApJ, 616, 966
Smith, M. A., Schlemmer, S., von Richthofen, J., & Gerlich, D. 2002, ApJ, 578, L87
Toomre, A. 1964, ApJ, 139, 1217
U, V., Medling, A., Sanders, D., et al. 2013, ApJ, 775, 115
Usero, A., García-Burillo, S., Fuente, A., Martín-Pintado, J., & Rodríguez-Fernández, N. J. 2004, A&A, 419, 897
Veilleux, S., Meléndez, M., Sturm, E., et al. 2013, ApJ, 776, 27
Veilleux, S., Rupke, D. S. N., Kim, D.-C., et al. 2009, ApJS, 182, 628
Wilson, C. D., et al. 2008, ApJS, 178, 189
Yun, M. S., & Scoville, N. Z. 1995, ApJ, 451, L45